



Publication Year	2018
Acceptance in OA@INAF	2020-10-01T15:27:20Z
Title	Mass-Richness Relations for X-Ray and SZE-selected Clusters at $0.4 < z < 2.0$ as þ Seen by Spitzer at $4.5 \text{ } \mu\text{m}$
Authors	Rettura, A.; Chary, R.; Krick, J.; ETTORI, STEFANO
DOI	10.3847/1538-4357/aad818
Handle	http://hdl.handle.net/20.500.12386/27537
Journal	THE ASTROPHYSICAL JOURNAL
Number	867



Mass–Richness Relations for X-Ray and SZE-selected Clusters at $0.4 < z < 2.0$ as Seen by *Spitzer* at $4.5 \mu\text{m}$

A. Rettura^{1,2} , R. Chary² , J. Krick², and S. Ettori³

¹ W. M. Keck Observatory, Kamuela, HI 96743, USA

² IPAC, Caltech, KS 314-6, Pasadena, CA 91125, USA

³ INAF, Osservatorio Astronomico di Bologna, via Ranzani 1, I-40127 Bologna, Italy

Received 2016 August 31; revised 2018 July 31; accepted 2018 August 1; published 2018 October 25

Abstract

We study the mass–richness relation of 116 spectroscopically confirmed massive clusters at $0.4 < z < 2$ by mining the *Spitzer* archive. We homogeneously measure the richness at $4.5 \mu\text{m}$ for our cluster sample within a fixed aperture of $2'$ radius and above a fixed brightness threshold, making appropriate corrections for both background galaxies and foreground stars. We have two subsamples, those which have (a) literature X-ray luminosities and (b) literature Sunyaev–Zel'dovich effect masses. For the X-ray subsample we re-derive masses adopting the most recent calibrations. We then calibrate an empirical mass–richness relation for the combined sample spanning more than one decade in cluster mass and find the associated uncertainties in mass at fixed richness to be ± 0.25 dex. We study the dependence of the scatter of this relation with galaxy concentration, defined as the ratio between richness measured within an aperture radius of 1 and 2 arcmin. We find that at fixed aperture radius the scatter increases for clusters with higher concentrations. We study the dependence of our richness estimates with depth of the $4.5 \mu\text{m}$ imaging data and find that reaching a depth of at least $[4.5] = 21$ AB mag is sufficient to derive reasonable mass estimates. We discuss the possible extension of our method to the mid-infrared *WISE* All Sky Survey data and the application of our results to the *Euclid* mission. This technique makes richness-based cluster mass estimates available for large samples of clusters at very low observational cost.

Key words: cosmology: observations – galaxies: clusters: general – galaxies: high-redshift – galaxies: statistics – infrared: galaxies – large-scale structure of universe

1. Introduction

Clusters of galaxies are the largest and most massive gravitationally bound systems in the universe. Clusters of galaxies are considered to be both unique astrophysical laboratories and powerful cosmological probes (e.g., White et al. 1993; Bartlett & Silk 1994; Viana & Liddle 1999; Borgani et al. 2001; Vikhlinin et al. 2009; Mantz et al. 2010; Rozo et al. 2010; Allen et al. 2011; Benson et al. 2013; Bocquet et al. 2015). Clusters grow from the highest density peaks in the early universe and thus their mass function is a tracer of the underlying cosmology (e.g., Press & Schechter 1974; Bahcall & Cen 1993; Gonzalez et al. 2012). Due to the steep dependence between number density and mass in the dark-matter halo mass function, deriving the cluster mass accurately is of paramount importance and large observational efforts have been devoted to this goal over the past three decades.

Different indirect methods, each of them leveraging unique observables of these systems, have been developed in the literature in order to weigh the most massive structures in the universe. These are (i) measuring the richness of a cluster, i.e., counting the number of galaxies associated with that cluster within a given radius (e.g., Abell 1958; Zwicky & Kowal 1968; Carlberg et al. 1996; Yee & López-Cruz 1999; Yee & Ellingson 2003; Rozo et al. 2009; Rykoff et al. 2012, 2014; Andreon & Congdon 2014; Andreon 2015, 2016; Saro et al. 2015; Melchior et al. 2017). (ii) Measuring the radial velocities of the cluster members, which yields the velocity dispersion of a cluster and can be used to derive the cluster's mass from the virial theorem, under the assumption that the structure is virialized (e.g., Girardi et al. 1996; Mercurio et al. 2003; Demarco et al. 2005, 2007). (iii) Measuring the intensity of the hot X-ray-emitting intracluster medium if this

gas is in hydrostatic equilibrium by factoring in its density and temperature distribution (e.g., Gioia et al. 1990; Vikhlinin et al. 1998; Böhringer et al. 2000; Pacaud et al. 2007; Šuhada et al. 2012; Ettori et al. 2013; Andreon et al. 2016). (iv) Measuring the inverse-Compton scatter of cosmic microwave background (CMB) photons off the energetic electrons in the hot intracluster gas. The resultant characteristic spectral distortion to the CMB is known as the Sunyaev–Zel'dovich effect (SZE; Sunyaev & Zeldovich 1972; Staniszewski et al. 2009; Hasselfield et al. 2013; Bleem et al. 2015; Planck Collaboration et al. 2015). (v) By measuring the coherent distortion that weak gravitational lensing produces on background galaxies, which has the advantage that it does not need prior knowledge on the baryon fraction of the cluster or its dynamical state (e.g., Bartelmann & Schneider 2001; Hoekstra 2007; Mahdavi et al. 2008; High et al. 2012; Hoekstra et al. 2012; Umetsu et al. 2014; von der Linden et al. 2014; Sereno 2015).

While there are large cluster samples selected from optical and near-infrared photometric surveys up to $z < 1.5$ (e.g., Gladders & Yee 2000; Koester et al. 2007; Hao et al. 2010; Menanteau et al. 2010; Brodwin et al. 2011; Wen et al. 2012; Ascaso et al. 2014; Rykoff et al. 2014; Bleem et al. 2015), in recent years, mid-infrared (MIR) photometric surveys with *Spitzer* have extended the landscape. The Infrared Array Camera (IRAC; Fazio et al. 2004) onboard the *Spitzer Space Telescope* has proven to be a sensitive tool for studying galaxy clusters. Ongoing *Spitzer* wide-area surveys are proving effective at identifying large samples of galaxy clusters down to low masses at $1.5 < z < 2$ (e.g., SDWFS, SWIRE, CARLA, SSSF; Eisenhardt et al. 2008; Papovich 2008; Wilson et al. 2009; Demarco et al. 2010; Galametz et al. 2010;

Stanford et al. 2012; Zeimann et al. 2012; Brodwin et al. 2013; Galametz et al. 2013; Muzzin et al. 2013; Wylezalek et al. 2013; Rettura et al. 2014), where current X-ray and SZE observations are restricted to only the most massive systems at these redshifts (Brodwin et al. 2011; Muzzin et al. 2013).

Even larger samples of clusters at $0.4 < z < 2.0$ will soon be available from upcoming and planned large-scale surveys like the Dark Energy Survey (DES; DES Collaboration et al. 2018), KiDS (de Jong et al. 2013), *Euclid* (Laureijs et al. 2011), LSST (LSST Science Collaboration et al. 2009), and *WFIRST*. However, until the next generation SZE instrumentation (e.g., ACTpol, SPTpol, SPT3G—in any case only covering the southern sky) or next generation X-ray telescopes (e.g., eRosita, Athena) become available, measuring the masses of the bulk of the high-redshift clusters at $0.4 < z \lesssim 2$ remains challenging.

In order to provide an efficient and reliable mass proxy for high-redshift clusters up to $z \sim 2$, in this paper, we calibrate a richness–mass relation using archival $4.5 \mu\text{m}$ data on a sample of published X-ray and SZE-selected clusters at $0.4 < z < 2.0$. At these redshifts, the $4.5 \mu\text{m}$ band traces rest-frame near-infrared light from the galaxies that is emitted by the high mass-to-light ratio stellar population. Thus, if the integrated mass function of galaxies is correlated with the cluster dark-matter halo in which they reside, the near-infrared richness should provide a reasonable tracer of cluster mass (e.g., Andreon 2006, 2013). This method of mass measurement has the advantage over the others described above because it is purely photometric, does not require a priori knowledge of the dynamical state of the cluster, and is observationally easy to obtain. We require only the cluster position, an approximate redshift estimate and at least 90 s depth coverage of IRAC $4.5 \mu\text{m}$ data over a single pointing of $5' \times 5'$ field of view.

The plan of the paper is as follows. In Section 2, we describe the archival cluster sample we have adopted throughout the work and describe how the cluster masses were derived. In Section 3, we present the *Spitzer* photometric cataloging procedure adopted. In Section 4, we present the definition of our richness indicator and study its dependence on survey depth and aperture radius adopted. In Section 5, we calibrate the mass–richness relation for each subsample individually and combined. In Section 6, we discuss our results, the possibility of extending our method to other MIR all-sky surveys, and the implication of our findings on future wide-field infrared surveys such as those that will be undertaken with *Euclid*. In Section 7, we summarize the results.

Throughout, we adopt a $\Omega_\Lambda = 0.7$, $\Omega_m = 0.3$, and $H_0 = 70 \text{ km s}^{-1} \text{ Mpc}^{-1}$ cosmology, and use magnitudes in the AB system.

2. Sample Selection

In the following section we present cluster samples drawn from the literature and the archival *Spitzer* data adopted in our analysis. Our aim is to assemble a large sample of clusters with known masses and redshifts for which archival IRAC data at $4.5 \mu\text{m}$ is publicly available. We define two cluster subsamples based on literature X-ray masses and literature SZE masses.

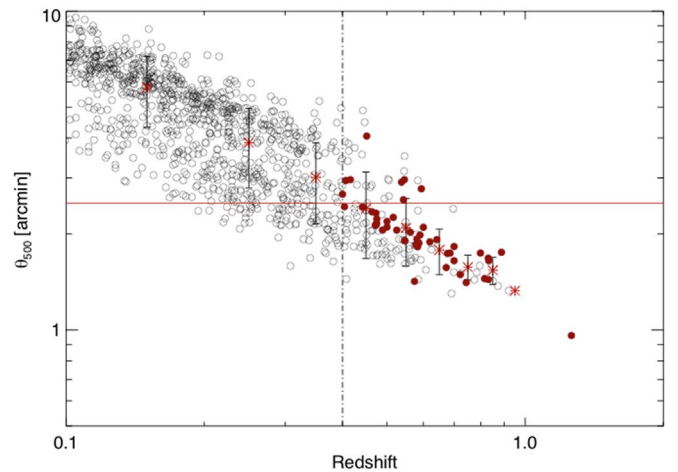


Figure 1. θ_{500} as a function of redshift for the entire MCXC sample of X-ray clusters. The horizontal red line indicates half the typical field of view of a single *Spitzer*/IRAC pointing. At $z > 0.4$ (dot-dashed line), the average θ_{500} of the sample is included in the *Spitzer*/IRAC field of view. Asterisks are average values in bins of redshift of size $\Delta z = 0.1$. The final X-ray sample analyzed in this study is indicated with solid red circles.

2.1. X-Ray Clusters Sample

The starting point for this sample is the Meta-catalog of X-ray detected clusters of galaxies (MCXC), a catalog of compiled properties of X-ray detected clusters of galaxies (Piffaretti et al. 2011, and references therein). This catalog is based on the *ROSAT* All Sky Survey (Voges et al. 1999) data on 1743 clusters at $0.003 < z < 1.261$ that have been homogeneously evaluated within the radius, R_{500} , corresponding to an overdensity of 500 times the critical density. For each cluster, the MCXC provides redshift,⁴ coordinates, R_{500} , and X-ray luminosity in the $0.1\text{--}2.4 \text{ keV}$ band, $L_{500,[0.1\text{--}2.4\text{keV}]}$. Based on the values published in Piffaretti et al. (2011), we also derive the angular size, $\theta_{500} = R_{500}/DA(z)$ for each cluster, where $DA(z)$ is the angular diameter distance.

In order to define a richness parameter to be used as a proxy for cluster mass, M_{500} , we need to define the aperture radius in which galaxies should be counted and the redshift range for which this radius is still representative of the cluster R_{500} . To this aim, in Figure 1, we show the entire MCXC sample θ_{500} versus redshift relation. The red horizontal line indicates the 2.5 arcmin radius of a single *Spitzer*/IRAC field of view. The red asterisks indicate the mean θ_{500} per redshift bin of $\Delta z = 0.1$, the error bars are the standard deviation of the mean per redshift bin. We note that at $z > 0.4$ (dot-dashed line) the average θ_{500} of the sample is included within the *Spitzer*/IRAC field of view. Therefore we adopt this lower redshift cut to the cluster samples considered in our study. There are 142 clusters in MCXC at $z > 0.4$.

The most reliable X-ray masses are obtained by solving the equation of hydrostatic equilibrium, which requires measurements of the density and temperature gradients of the X-ray emitting gas (see discussion in Maughan 2007). This is only possible for nearby bright clusters, therefore it remains a challenge for the majority of clusters detected in X-ray surveys, especially at high redshifts where surface brightness dimming effects become significant. Thus, in most cases, cluster masses are estimated from simple properties such as X-ray luminosities

⁴ Typical redshift uncertainty is $\sigma_z < 0.001$ (see discussion in Liu et al. 2015).

(L_X) or from adopting a single global temperature (kT) via the calibration of scaling relations.

To derive an estimate of the total cluster mass, M_{500} , within R_{500} , we adopt the most recent calibrations, in particular in their redshift evolution, of the relations between X-ray global properties and cluster total mass, as presented in Reichert et al. (2011). Reichert et al. (2011, see also references therein) obtained these relations by homogenizing published estimates of X-ray luminosity and total mass. These values were rescaled at different radii and overdensities by using their dependence upon the gas density, which was described by a β -model (Cavaliere & Fusco-Femiano 1976).

Reichert et al. (2011) scaling relations, together with the MCXC luminosities, are then used here to run the following iterative process: (i) an input temperature is assumed; (ii) a conversion from the MCXC $L_{500,[0.1-2.4\text{keV}]}$ luminosity to the pseudo-bolometric (0.01–100 keV) value, $L_{500,\text{bol}}$, is derived assuming the thermal `apecc` model in XSPEC (Arnaud 1996), adopting the temperature assumed at step (i) and a metal abundance of 0.3 times the solar value; (iii) a value of the mass within an overdensity of 500 with respect to the critical density of the universe at the cluster’s redshift is then calculated from Equation (26) in Reichert et al. (2011),

$$\frac{M_{500,X}}{10^{14} M_{\odot}} = (1.64 \pm 0.07) \cdot \left(\frac{L_{500,\text{bol}}}{10^{44} \text{ erg s}^{-1}} \right)^{0.52 \pm 0.03} \cdot \left(\frac{H(z)}{H_0} \right)^{\alpha}, \quad (1)$$

where $H(z) = \sqrt{\Omega_{\Lambda} + \Omega_m^*(1+z)^3 + \Omega_k^*(1+z)^2}$, $\Omega_k = (1 - \Omega_m - \Omega_{\Lambda})$, and $\alpha = -0.90_{-0.15}^{+0.35}$,

(iv) a new temperature is recovered from the M – T relation (Equation (23) in Reichert et al. 2011) and compared to the input value assumed at step (i); (v) the calculations are repeated if the relative difference between these two values is larger than 5%.

We consider also a correction on the given luminosity due to the change in the initial R_{500} . This correction, typically a few percent, is obtained as described in Piffaretti et al. (2011), by evaluating the relative change of the square of the gas density profile integrated over the cylinder with dimension of $r = R_{500}$ and height of $2 \times 5 R_{500}$.

As a consistency test, for a subsample of common clusters, we can also compare the bolometric luminosities we have obtained with those independently derived by Maughan et al. (2012). Maughan et al. (2012) used a sample of 115 galaxy clusters at $0.1 < z < 1.3$ observed with *Chandra* to investigate the relation between X-ray bolometric luminosity and Y_X (the product of gas mass and temperature) and found a tight L_X – Y_X relation (Maughan 2007). They also demonstrate that cluster masses can be reliably estimated from simple luminosity measurements in low quality data where direct masses, or measurements of Y_X , are not possible.

There are 26 clusters in common between our *ROSAT*-based sample and their *Chandra* sample. In Figure 2, we compare the bolometric luminosities obtained independently and find the values to be in very good agreement.

We then searched for *Spitzer*/IRAC archival observations homogeneously covering at least an area within a 2.5 arcmin radius from the cluster center coordinates and with a minimum exposure time of 90 s. This depth ensures that we reach at least

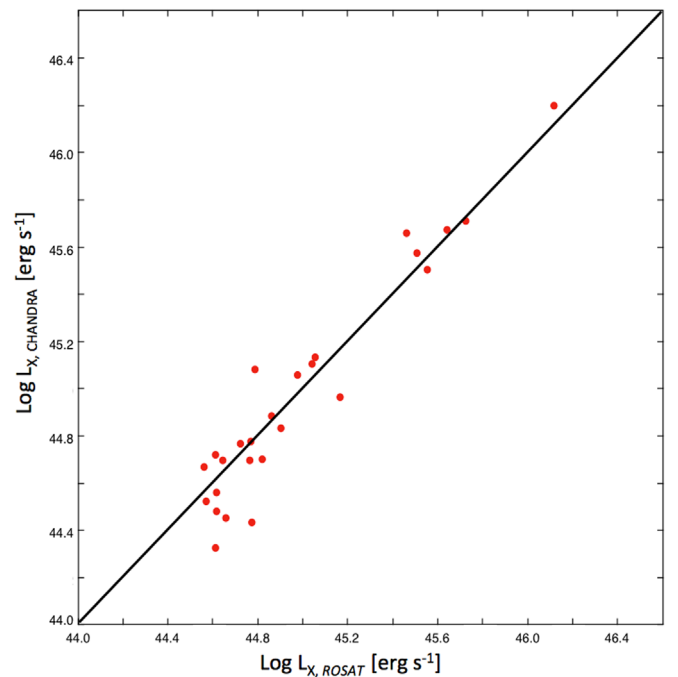


Figure 2. *ROSAT*-based bolometric luminosities derived in this work are plotted against those measured with *Chandra* by Maughan et al. (2012) for a subsample of 26 clusters in common.

a 5σ sensitivity limit of 21.46 AB mag (9.4 μJy) at $4.5 \mu\text{m}$ (see Section 3.1 for further discussion of required depth).

These requirements result in a final X-ray-selected sample comprised of 47 galaxy clusters at $0.4 < z < 1.27$ (indicated by red circles in Figure 1). We note that a few large clusters (indicated by red circles above the red line in Figure 1) have still been considered throughout this work. This is because the mean θ_{500} in those redshift bins is smaller than the IRAC field of view. It also ensures an adequate sample size and avoids biasing our derived richness–mass relation against large, less-concentrated clusters. The derived cluster mass and redshift distributions of our X-ray sample are illustrated in Figure 3 (blue circles and histograms).

2.2. SZE Clusters Sample

Recent years have seen rapid progress of both the quality and quantity of SZE measurements using a variety of instruments. Therefore, several programs have been launched in the past few years with the aim of measuring total masses through the SZ effect of large samples of clusters, both for cosmology and astrophysics studies. *Spitzer*/IRAC data coverage over some of the SZ survey fields have been requested, as well as targeted SZE observations of existing MIR-selected clusters have also been obtained by various investigators.

We have therefore mined the *Spitzer*/IRAC archive and drawn a heterogeneous sample of spectroscopically confirmed SZE-selected clusters based from a number of these programs. Applying the same redshift and photometric coverage selection criteria illustrated in Section 2.1, the final SZE-selected sample considered in our study is comprised of 69 galaxy clusters at $0.4 < z < 2.0$.

In particular, our sample is comprised of 4 clusters from the *Planck* Cluster Catalog (Planck Collaboration et al. 2015), 4 clusters from the Massive Distant Clusters of *WISE* Survey (MADCoWS, Brodwin et al. 2015), 1 cluster from the IRAC

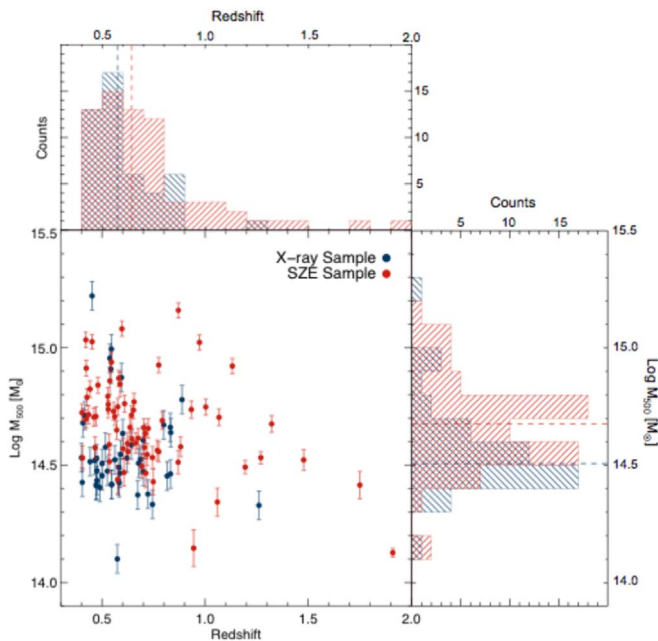


Figure 3. Cluster mass and redshift distributions of the X-ray- (blue) and SZE-selected (red) cluster samples studied in this work. Both subsamples extend over similar ranges of the M_{500-z} plane, and the median values are indicated by the dashed lines of the corresponding color.

Distant Cluster Survey (IDCS, Brodwin et al. 2012), 1 cluster from the *XMM-Newton* Large Scale Structure Survey (XLSSU, Pierre et al. 2011; Mantz et al. 2014), and 59 clusters from the SPT-SZ Cluster Survey (SPT-SZ, Bleem et al. 2015).

Cluster masses, $M_{500,SZ}$, as reported in the aforementioned papers, are based on the spherically integrated Comptonization measurement, $Y_{500,SZ}$, obtained by either the *Planck Space Telescope*, the Combined Array for Research in Millimeter-wave Astronomy (CARMA⁵), or the South Pole Telescope (SPT; Carlstrom et al. 2011; Austermann et al. 2012; Story et al. 2013). Cluster mass and redshift distributions of the final SZE-selected subsample are illustrated in Figure 3 (red circles and histograms) and can be compared with the X-ray sample shown therein.

We also note that only five clusters in our sample, Clus ID 26, 355, 621, 1050, and OBJ8 have mass estimates in the literature, derived both from L_X and $Y_{500,SZ}$, and that with the exception of Clus ID 621, 1050, the majority have consistent mass estimates within 2σ of the associated errors.

3. *Spitzer* Data

Publicly available *Spitzer*/IRAC data for each cluster in our sample is accessible via the *Spitzer Heritage Archive* (SHA). All of the IRAC data for the X-ray-selected sample were acquired during the initial cryogenic mission, while all but four of the SZE sample data were acquired during the post-cryogenic *Warm Mission*. The *Warm* and *Cryo* missions have been put onto the same calibration scale in the SHA provided data products, so we expect no differences between the missions to be relevant to this work.

3.1. Source Extraction

The publicly accessible *Spitzer* Enhanced Imaging Products⁶ (SEIP) provide super mosaics (combining data from multiple programs where available) and a source list of photometry for sources observed during the cryogenic mission of *Spitzer*. The SEIP includes data from the four channels of IRAC (3.6, 4.5, 5.8, 8 μm) and the 24 μm channel of the Multi-Band Imaging Photometer for *Spitzer* (MIPS) where available. In addition to the *Spitzer* photometry, the source list also contains photometry for positional counterparts found in the AllWISE release of the *Wide-Field Infrared Survey Explorer* (WISE) and in the Two Micron All Sky Survey (2MASS). To ensure high reliability, strict cuts were placed on extracted sources and some legitimate sources may appear to be missing. These sources were removed by cuts in size, compactness, blending, shape, and SNR, along with multiband detection requirements. In most fields, the completeness of the source list is well matched to expectations for a SNR = 10 cutoff, as reliability is favored over completeness. However, the list may be incomplete in areas of high surface brightness and/or high source surface density. This is most relevant for this work for objects near bright sources or the centers of clusters, which may have a higher source density.

Following the recommendations in Surace et al. (2004), for our richness estimate we adopt the aperture corrected IRAC 4.5 μm flux density measured within an aperture of diameter 3.8 arcsec from the SEIP source list. The chosen aperture is twice the instrumental FWHM, which provides accurate photometry with an aperture correction for a point source already applied, which is customary for cluster studies with *Spitzer* in the literature (e.g., Bremer et al. 2006; Rettura et al. 2006). IRAC PSF has a FWHM ~ 2 arcsec, thus we note that a star/galaxy separation in *Spitzer* data, especially at faint fluxes, is not straightforward. Therefore we will describe in Section 4 how we account and correct for foreground stars in our richness estimates.

For the *Warm Mission* data, a SEIP source list is not available in the *Spitzer* archive. However, we have adopted the same SEIP source extraction pipeline and applied it ourselves in exactly the same way as for the *Cryo* mission clusters.

3.2. Survey Depth

As we deal with a heterogeneous sample that has been observed by *Spitzer* at varying depths, for consistency of our analysis, we aim to be able to calibrate our method to a depth that is reached by all our archival data.

For illustration purposes, we show in Figure 4 the number counts of four representative clusters in our samples along with the number counts derived from a reference deep *Spitzer* legacy program that we adopt as a control field. The *Spitzer* UKIDSS Ultra Deep Survey (SpUDS, PI: J. Dunlop) data used here come from a program covering ~ 1 deg² in the UKIRT Infrared Deep Sky Survey, Ultra Deep Survey field (UKIDSS UDS Dye et al. 2006), centered at R.A. = 02^h:18^m:45^s, Decl. = $-05^{\circ}:00':00''$. Note that we use the SEIP source list photometry available in the archive for our control (SpUDS) field as well. The SpUDS survey reaches greater sensitivities than the data on the majority of our clusters, in particular for the SZE

⁵ <https://www.mmarray.org>

⁶ <http://irsa.ipac.caltech.edu/data/SPITZER/Enhanced/SEIP>

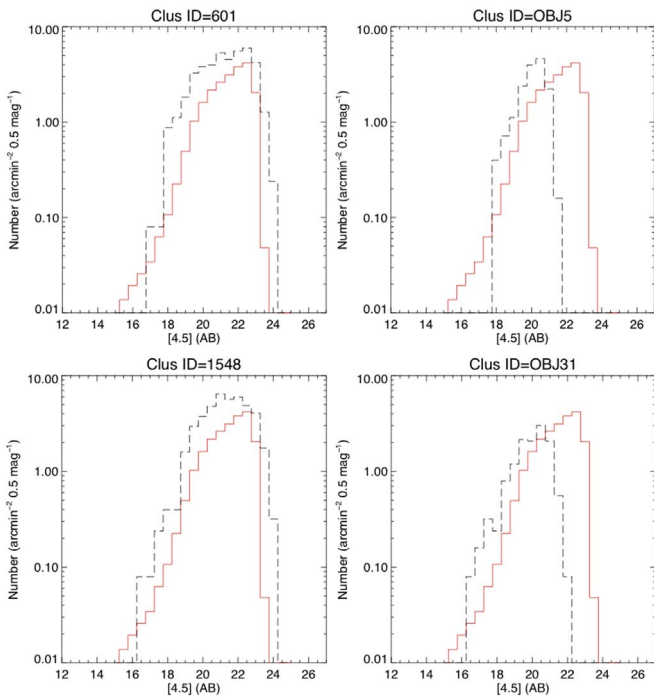


Figure 4. $4.5 \mu\text{m}$ number counts for four representative clusters in our sample (black dashed histogram) compared to number counts of the deeper SpUDS control field (red solid histogram). The left column shows the number counts for two X-ray clusters while the right column shows the number counts for two SZE clusters.

sample, as shown by examples on the right column of the panel Figure 4.

As shown in Figure 5 for the entire sample, the IRAC coverage of our samples is not uniform. The median depth of the SZE cluster observations reach $[4.5] = 21$ AB, for instance, while the median depth for the X-ray sample reaches $[4.5] = 22.5$ AB. For the sake of overall consistency of our analysis and to be able to calibrate our method to a depth that the vast majority of current and future *Spitzer* surveys can easily reach (with even 90 s exposure), we adopt $[4.5]_{\text{cut}} = 21$ AB as the magnitude cut for all subsequent analyses. We will also further investigate the dependence of richness estimates on image depth in Section 4.1.

For galaxy stellar populations formed at high redshift, a negative k-correction provides a nearly constant $4.5 \mu\text{m}$ flux density over a wide redshift range. An $L_{[4.5]}^*$ galaxy formed at $z_f = 3$ will have $[4.5] \sim 21$ (AB) at $0.4 \lesssim z \lesssim 2.0$, which is sufficiently bright that it is robustly seen in even just 90 s integrations with *Spitzer* (e.g., Eisenhardt et al. 2008).

While we recognize that using the simple approach of a single apparent magnitude cut at $0.4 < z < 2.0$ would introduce a bias for optical mass–richness relationships, we note here that an infrared relation is not significantly affected because of the k-correction. Adopting Mancone et al. (2010) results on the evolution with redshift of the characteristic absolute magnitude $M_{[4.5]}^*(z)$, we note that at $4.5 \mu\text{m}$, in the redshift range spanned by our sample, the stellar population evolution and redshift evolution are roughly matched, thus sampling a similar rest-frame luminosity range of the cluster galaxy population as a function of redshift. Because of cluster galaxy population evolution with redshift seen through the $4.5 \mu\text{m}$ band filter at $0.4 \lesssim z \lesssim 2$, our adopted apparent magnitude limit $[4.5]_{\text{cut}}$ always corresponds to a roughly

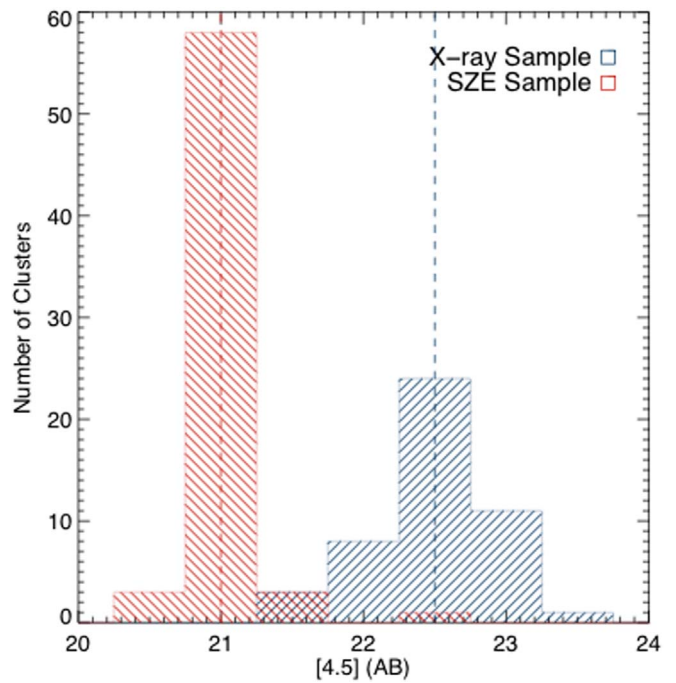


Figure 5. Histogram of the $4.5 \mu\text{m}$ depths reached by the archival data available for the X-ray (blue) and the SZE (red) samples. The dashed lines indicate the median depth of each sample.

similar absolute magnitude $M_{[4.5]_{\text{cut}}} \sim M_{[4.5]}^*(z) + 1$ over this large redshift range. We find in fact that $M_{[4.5]_{\text{cut}}}$ varies between $M_{[4.5]}^*(z) + 0.87$ (at $z \gtrsim 1.2$) and $M_{[4.5]}^*(z) + 1.17$ (at $z \sim 0.5$), thus by 0.3 mag. This small variation in limit magnitude will not significantly increase the scatter in the mass–richness relation we will derive in the next Section 5. In Section 4.1, based on a subsample of clusters for which deeper data are available, we will study the dependence of richness estimates on survey depth and will parameterize a linear relation (Equation (3)) to account for these effects. Accordingly, a variation in magnitude cut by 0.3 mag will result in a variation in richness, $\Delta R \sim 6 \text{ gals} \times \text{Mpc}^{-2}$, hence in logarithmic scale $\Delta \text{Log } R \sim 0.05$, which is very small and will not significantly increase the scatter in the derived mass–richness relation.

4. Derivation of *Spitzer* $4.5 \mu\text{m}$ Richness

The richness of a cluster is a measure of the surface density of galaxies associated with that cluster within a given radius. Because of the presence of background and foreground field galaxies and foreground stars, one cannot identify which source in the vicinity of a cluster belongs to the cluster. Richness is therefore a statistical measure of the galaxy population of a cluster, based on some operational definition of cluster membership and an estimate of foreground/background subtraction. Furthermore, as we aim to provide an efficient and inexpensive $4.5 \mu\text{m}$ photometric proxy of cluster mass within R_{500} , we need to adopt a sufficiently large aperture radius in which galaxies should be counted in a way that minimizes the Poisson scatter in richness and takes into account the typical R_{500} of clusters at $z > 0.4$ and the angular size constraint defined by the single pointing *Spitzer* field of view. Thus we define a richness parameter, $R_{[4.5]}$, as the background-subtracted projected surface density of sources with $[4.5] < 21$

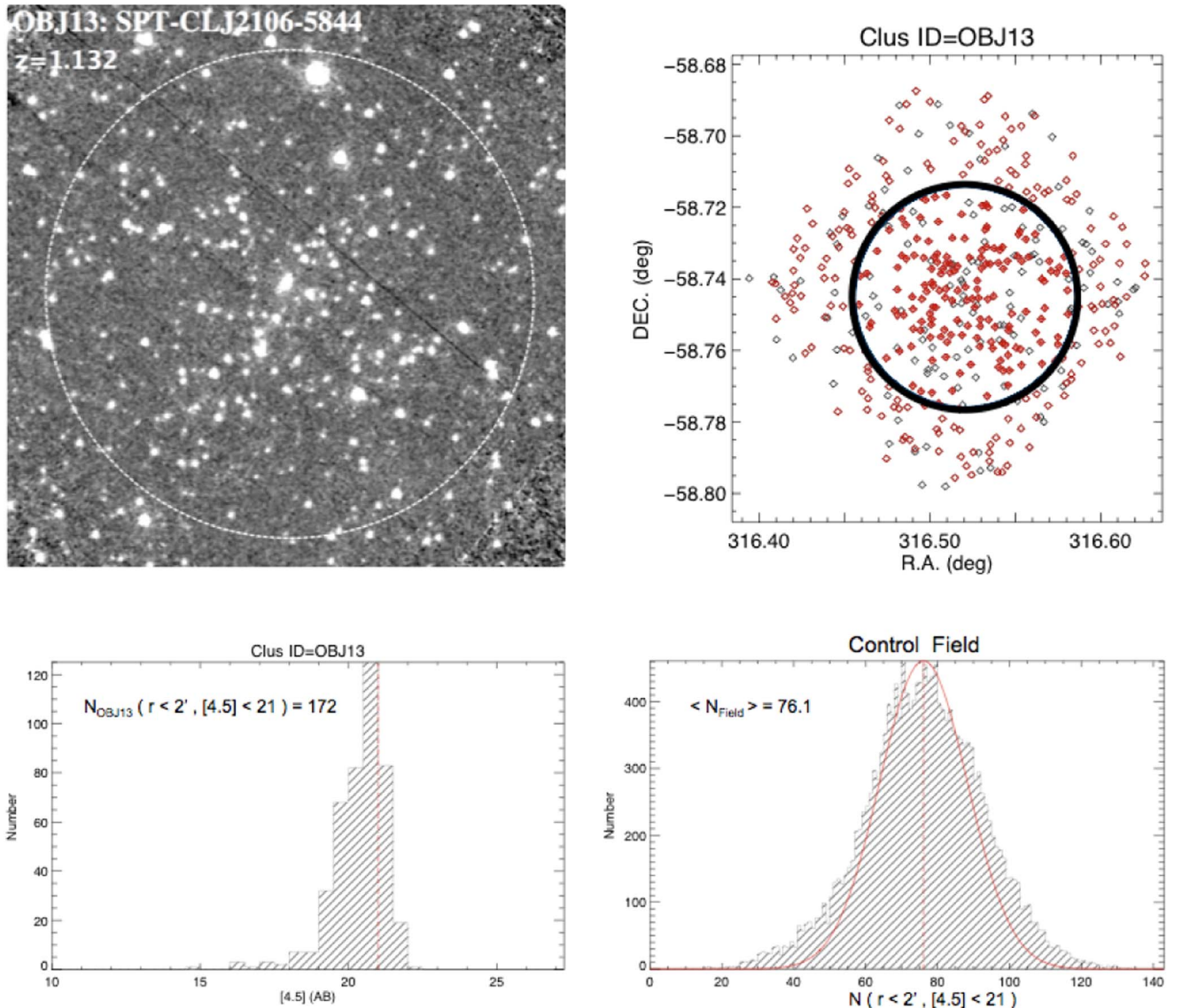


Figure 6. Top left panel: [4.5]-band image of a representative cluster in our sample at $z = 1.132$. The white dashed circle indicated has a radius $r = 2'$. Top right panel: positions of all the sources extracted by the photometric pipeline from the $4.5 \mu\text{m}$ band image of the cluster and indicated by black diamonds. Sources with magnitudes $[4.5] < 21$ AB are indicated by open red diamonds. The black circle has a radius $r = 2'$, centered on the reported cluster center. Magnitude-selected sources that are also within the circle are indicated with filled red symbols. Bottom left panel: [4.5] magnitude distribution of all sources in the *Spitzer*/IRAC image of this cluster. The red dotted-dashed line indicates the magnitude cut adopted consistently throughout this work. The number of sources, N_{Cluster} , brighter than the $[4.5]_{\text{cut}} = 21$ AB and within $2'$ from the cluster center is indicated. Bottom right panel: distribution of the number of sources in the control field brighter than $[4.5] = 21$ and within $r < 2'$ from each source extracted in the SpUDS photometric catalog. The red line indicates a 2σ clipped Gaussian fit of the distribution. The red dotted-dashed line indicates the mean of the Gaussian fit, $\langle N_{\text{Field}} \rangle$, which is used for the source background correction throughout this work, as described in the text. Clearly, the cluster field has more than twice as many objects within the aperture.

AB within 2 arcmin from the cluster center, expressed in units of galaxies Mpc^{-2} .

We first measure the number of objects in the vicinity of the cluster, N_{Cluster} , with $[4.5] < 21$ mag within 2 arcmin of the cluster center determined from the SZE or X-ray data (bottom-left panel of Figure 6). In order to estimate the number of background sources (stars and galaxies) to subtract, we use the SpUDS survey to derive a mean blank-field surface density of sources above the same magnitude limit. To estimate this, we measure the number of sources above the magnitude limit within an aperture radius of 2 arcmin from each source with $[4.5] < 21$ in the SEIP photometric catalog of the SpUDS field. We then fit a Gaussian to the distribution, iteratively clipping at 2σ (see the bottom-right panel of Figure 6). The resulting mean of the distribution, $\langle N_{\text{Field}} \rangle = 76$ gals, is then subtracted from N_{Cluster} .

This method of background subtraction assumes that the stellar density in the SpUDS field is the same as that in the cluster field, which need not be true due to the structure of our galaxy. As we deal with an all-sky archival sample of clusters, we correct for the variation of the foreground star counts with Galactic latitude. Using the Wainscoat et al. (1992) mode predictions⁷ for the IR point-source sky, we can estimate the number of stars with $[4.5] < 21$ within 2 arcmin from the center of each cluster in our sample, N_S , and compare it to the average value for the SpUDS field, $N_{S,\text{Field}} = 9.4$. Thus we can correct our richness estimate at the location of each cluster for the difference in star counts by

⁷ Web tool available at <http://irsa.ipac.caltech.edu/applications/BackgroundModel/>.

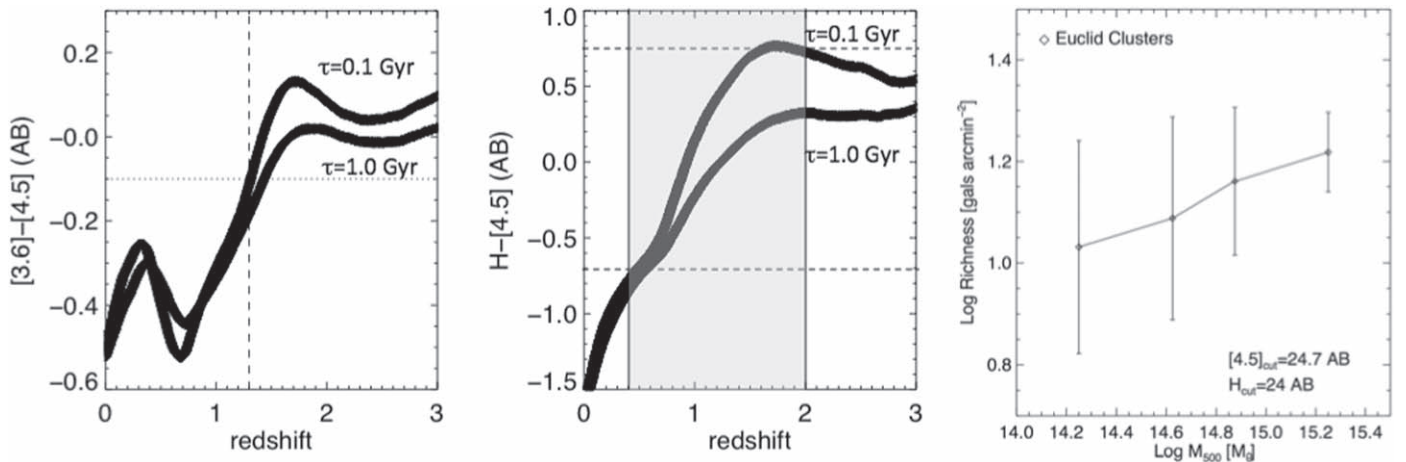


Figure 7. Evolution of the $[3.6]-[4.5]$ color (left panel) and $H-[4.5]$ color (middle panel) with redshift for a set of Bruzual & Charlot (2003) stellar population models with exponentially declining star-formation rates with $\tau = 0.1$ Gyr (early-type galaxy) and $\tau = 1.0$ Gyr (star forming galaxy). These colors are used to translate our measure of $[4.5]$ μm richness into a H -band richness estimate. The right panel shows the predicted richness (in gals arcmin^{-2}) for *Euclid* clusters at $0.4 < z < 2.0$, in the wide-area survey ($H_{\text{cut}} = 24$ AB) as a function of cluster mass.

subtracting the difference between these numbers:

$$R_{[4.5]} = N_{\text{Cluster}} - \langle N_{\text{Field}} \rangle - (N_S - N_{S,\text{Field}}), \quad (2)$$

where values N_{Cluster} and N_S for each cluster in our sample are listed in Tables 1 and 2.

To test the fidelity of the calibrated model of the galaxy adopted here, we have also compared Wainscoat et al. (1992) predictions with the ones from a more recent model of the galaxy, TRILEGAL (Girardi et al. 2012). At each of the 116 cluster positions, TRILEGAL has been run 10 times with varying input parameters (IMFs, extinction laws, model of the thin/thick disk, halo and bulge model) to output the mean and stdev values for the number of stars within 2 arcmin. We find the results of the two models in remarkably good agreement. At the coordinates of our sample clusters, we find the median difference between the outputs of the two models to be only ~ 1.5 stars in a 2 arcmin radius. The mean difference of the two models is found to be ~ 4.3 stars in a 2 arcmin radius. This difference is two orders of magnitude smaller than the typical total source counts, N_{Cluster} , at the location of the clusters (see Tables 1 and 2) and is hence negligible with respect to the typical errors (Poissonian statistics) reported here.

Finally we normalize for the surface area subtended by the $2'$ radius aperture at the redshift of each cluster and express $R_{[4.5]}$ in units of gals Mpc^{-2} throughout the paper (unless specified). We note that since projected areas evolve slowly with redshift, in particular at high redshift, our method is also suitable for clusters for which only a photometric redshift is available. For instance, for a $z_{\text{phot}} = 1.0$ cluster, even a large uncertainty in redshift of $\Delta z = \pm 0.1$ would only result in a variation of area of just $\sim 5\%$, implying a small variation of the inferred $R_{[4.5]}$.

The derived richness values for our sample of clusters are listed in Tables 1 and 2. Richness uncertainties account for Poisson fluctuations in background counts and cluster counts as well as the uncertainty in the mean background counts shown in Figure 6.

We note that we do not adopt a color criterion in our richness definition. The $[3.6]-[4.5]$ color is known to be degenerate with redshift at $z \lesssim 1.3$, but can be used as an effective redshift indicator (e.g., Papovich 2008; Muzzin et al. 2013; Wylezalek et al. 2013; Rettura et al. 2014) at $z > 1.3$. The method takes advantage of the fact that the $[3.6]-[4.5]$ color is a linear function of redshift between $1.3 \lesssim z \lesssim 1.5$ and at $z \gtrsim 1.5$ the color reaches a plateau out to $z \sim 3$ (see also left panel of Figure 7). While an IRAC

color cut $[3.6]-[4.5] > -0.1$ (AB) is effective at identifying galaxies at $z > 1.3$, due to the color degeneracy at lower redshifts, having at least one shallow optical band in addition, would be required for alleviating contamination from foreground interlopers at $z < 0.3$ (see discussion in Muzzin et al. 2013). Since optical data are unavailable for the large part of our archival sample and $>90\%$ of our sample is comprised of cluster galaxies at $z < 1.3$ we do not include a color cut in our definition of richness. We also note that by measuring richness at $4.5 \mu\text{m}$, corresponding to rest-frame near-infrared bands at the redshifts spanned by our sample, we are tracing the masses of galaxies better than optical richness estimates because stellar mass-to-light ratios show less scatter in the NIR than in the optical (e.g., Bell & de Jong 2001).

We remind that our method is based on counts in cells centered on either the X-ray or the SZE central positions as reported in the literature. As current and future *Spitzer*-selected cluster survey may adopt our method to estimate a mass proxy as well, it is valuable to attempt to estimate how using instead *Spitzer*-determined cluster centers would affect the richness estimation, hence the derived cluster mass estimates.

To test the effect of miscentering on richness estimates we have blindly determined cluster centers from *Spitzer* data directly in a field where samples of confirmed spectroscopic clusters had also published X-ray derived centers. In our test we implemented the similar cluster finding and centering algorithm described in Rettura et al. (2014) and ran a cluster search on the *Spitzer* data of the Bootes field (SDWFS; Ashby et al. 2009).

We identify five infrared selected clusters associated to spectroscopically confirmed clusters at $1.3 < z < 1.75$, where X-ray data are also available in the literature (Brodwin et al. 2011, 2013, 2016). We measure the mean positional offset, Δ_{pos} , of the newly derived *Spitzer* centers with respect to the published center coordinates. We find $\Delta_{\text{pos}} = 0'.2 \pm 0'.1$. We then shift the centers of all the clusters in this paper in a random direction by Δ_{pos} and derive new $R_{[4.5]\text{shift}}$ values. We find the mean inferred number of objects in the vicinity of the shifted cluster position, $N_{\text{cluster,shift}}$, to vary by 8% with respect to the previous N_{cluster} estimates reported in Tables 1 and 2. Using Equation (2), this translates to a difference in $R_{[4.5]}$ on the order of 0.06 dex, which is more than a factor of four smaller than our estimated uncertainties in mass at fixed richness.

Table 1
X-Ray Selected Cluster Sample

Clus ID	R.A. (deg., J2000)	Decl. (deg., J2000)	NAME	z	$\log M_{500,X}$ (M_{\odot})	$\log R_{[4.5]}$ (galaxies Mpc^{-2})	N_{Cluster}	N_S
26	4.6408	16.4381	MACS J0018.5+1626	0.5456	14.995 \pm 0.035	1.645 $^{+0.061}_{-0.071}$	162	14.32
46	7.64	26.3044	WARP J0030.5+2618	0.5	14.506 \pm 0.029	1.716 $^{+0.056}_{-0.065}$	173	19.31
51	8.9971	85.2214	WARP J0035.9+8513	0.8317	14.462 \pm 0.034	1.721 $^{+0.056}_{-0.064}$	242	37.17
145	25.3846	-30.5783	400d J0141-3034	0.442	14.514 \pm 0.028	1.604 $^{+0.064}_{-0.074}$	134	8.74
156	28.1721	-13.9703	WARP J0152.7-1357	0.833	14.638 \pm 0.035	1.448 $^{+0.075}_{-0.091}$	149	8.60
187	34.1404	-17.7908	WARP J0216.5-1747	0.578	14.435 \pm 0.030	1.119 $^{+0.106}_{-0.140}$	101	8.75
200	37.6108	18.6061	400d J0230+1836	0.799	14.671 \pm 0.035	1.520 $^{+0.070}_{-0.083}$	167	15.70
268	52.1504	-21.6678	400d J0328-2140	0.59	14.545 \pm 0.031	1.819 $^{+0.050}_{-0.057}$	208	10.59
276	53.2925	-24.9447	400d J0333-2456	0.475	14.477 \pm 0.029	1.459 $^{+0.074}_{-0.089}$	123	10.73
312	58.9971	-37.6961	400d J0355-3741	0.473	14.528 \pm 0.029	1.683 $^{+0.058}_{-0.067}$	155	12.39
316	61.3512	-41.0042	400d J0405-4100	0.686	14.524 \pm 0.032	1.525 $^{+0.069}_{-0.082}$	156	13.23
355	73.5462	-3.015	MACS J0454.1-0300	0.5377	14.954 \pm 0.034	1.676 $^{+0.059}_{-0.068}$	178	25.66
380	80.2937	-25.51	400d J0521-2530	0.581	14.491 \pm 0.030	1.357 $^{+0.083}_{-0.102}$	135	23.86
382	80.5575	-36.4136	400d J0522-3624	0.472	14.412 \pm 0.028	1.589 $^{+0.065}_{-0.076}$	150	22.29
405	85.7117	-41.0014	RDCS J0542-4100	0.642	14.585 \pm 0.032	1.552 $^{+0.067}_{-0.080}$	170	26.83
550	132.1983	44.9392	RX J0848.7+4456	0.574	14.100 \pm 0.028	1.375 $^{+0.081}_{-0.100}$	126	13.56
551	132.2346	44.8711	RX J0848.9+4452	1.261	14.328 \pm 0.041	0.889 $^{+0.133}_{-0.193}$	105	13.54
557	133.3058	57.9956	400d J0853+5759	0.475	14.435 \pm 0.028	1.683 $^{+0.058}_{-0.067}$	157	14.01
586	141.6521	12.7164	400d J0926+1242	0.489	14.405 \pm 0.028	1.567 $^{+0.066}_{-0.078}$	141	14.00
601	145.7796	46.9975	RXC J0943.1+4659	0.4069	14.679 \pm 0.030	1.939 $^{+0.044}_{-0.049}$	192	10.53
621	149.0121	41.1189	400d J0956+4107	0.587	14.465 \pm 0.030	1.322 $^{+0.086}_{-0.107}$	118	9.88
631	150.5321	68.98	400d J1002+6858	0.5	14.455 \pm 0.029	1.568 $^{+0.066}_{-0.078}$	142	13.35
634	150.7671	32.9078	400d J1003+3253	0.4161	14.711 \pm 0.030	1.830 $^{+0.050}_{-0.056}$	168	9.63
713	164.2479	-3.6244	MS1054.4-0321	0.8309	14.661 \pm 0.035	1.454 $^{+0.075}_{-0.090}$	154	12.61
743	169.375	17.7458	400d J1117+1744	0.547	14.417 \pm 0.029	1.525 $^{+0.069}_{-0.082}$	137	8.73
747	170.0321	43.3019	WARP J1120.1+4318	0.6	14.634 \pm 0.032	1.547 $^{+0.068}_{-0.080}$	146	8.31
748	170.2429	23.4428	400d J1120+2326	0.562	14.522 \pm 0.030	1.647 $^{+0.061}_{-0.071}$	159	8.37
825	180.5571	57.8647	400d J1202+5751	0.677	14.508 \pm 0.032	1.372 $^{+0.081}_{-0.100}$	129	9.45
864	185.3542	49.3019	400d J1221+4918	0.7	14.605 \pm 0.033	1.580 $^{+0.065}_{-0.077}$	163	8.55
865	185.5079	27.1553	400d J1222+2709	0.472	14.417 \pm 0.028	1.522 $^{+0.069}_{-0.083}$	127	8.11
873	186.74	33.5472	WARP J1226.9+3332	0.888	14.779 \pm 0.038	1.281 $^{+0.089}_{-0.113}$	127	8.02
971	198.0808	39.0161	400d J1312+3900	0.404	14.426 \pm 0.027	1.688 $^{+0.058}_{-0.067}$	139	8.48
1020	203.585	50.5181	ZwCl 1332.8+5043	0.62	14.530 \pm 0.031	1.682 $^{+0.058}_{-0.068}$	176	9.29
1050	206.875	-11.7489	RXC J1347.5-1144	0.4516	15.221 \pm 0.037	1.726 $^{+0.056}_{-0.064}$	162	15.81
1063	208.57	-2.3628	400d J1354-0221	0.546	14.418 \pm 0.029	1.687 $^{+0.058}_{-0.067}$	169	12.94
1066	209.3308	62.545	400d J1357+6232	0.525	14.474 \pm 0.029	1.635 $^{+0.061}_{-0.072}$	154	11.18
1089	213.7962	36.2008	WARP J1415.1+3612	0.7	14.473 \pm 0.032	1.498 $^{+0.071}_{-0.085}$	149	9.61
1094	214.1171	44.7772	NSCS J141623+444558	0.4	14.531 \pm 0.028	1.778 $^{+0.053}_{-0.060}$	154	9.77
1107	215.9492	24.0781	MACS J1423.8+2404	0.543	14.909 \pm 0.034	1.642 $^{+0.061}_{-0.071}$	157	10.25
1171	229.4829	31.4597	WARP J1517.9+3127	0.744	14.332 \pm 0.032	1.033 $^{+0.115}_{-0.158}$	105	12.11
1184	231.1679	9.9597	WARP J1524.6+0957	0.516	14.576 \pm 0.030	1.522 $^{+0.069}_{-0.083}$	140	15.69
1264	250.4679	40.0247	400d J1641+4001	0.464	14.520 \pm 0.029	1.564 $^{+0.066}_{-0.078}$	142	18.84
1410	275.4087	68.4644	RX J1821.6+6827	0.8156	14.453 \pm 0.034	1.135 $^{+0.104}_{-0.137}$	132	29.93
1506	309.6225	-1.4214	RX J2038.4-0125	0.673	14.373 \pm 0.031	1.208 $^{+0.096}_{-0.124}$	165	62.22
1519	314.0908	-4.6308	MS2053.7-0449	0.583	14.425 \pm 0.030	1.799 $^{+0.052}_{-0.058}$	231	40.92
1548	322.3579	-7.6917	MACS J2129.4-0741	0.594	14.873 \pm 0.034	1.652 $^{+0.060}_{-0.070}$	181	24.79
1658	345.7004	8.7306	WARP J2302.8+0843	0.722	14.377 \pm 0.031	1.158 $^{+0.102}_{-0.133}$	117	16.19

Note. $M_{500,X}$ values as reported by Piffaretti et al. (2011).

4.1. Dependence of Richness on Survey Depth and Aperture Radius

In order to investigate the effect of the chosen aperture radius and depth of the IRAC 4.5 μm data on richness estimates, we performed a series of tests on a subsample of clusters where the IRAC data is deep enough to allow us to measure richness values at different sensitivity levels. As shown in Figure 5, the

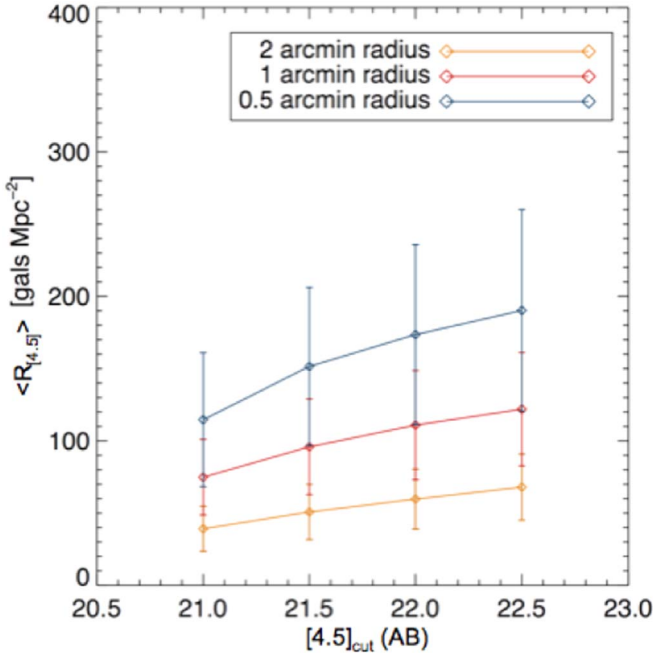
X-ray sample contains a “deep” subsample of 36 clusters for which their depth is ≥ 22.5 mag AB. We measure the average (and standard deviation of the mean) richness of this sample down to various depths, $[4.5]_{\text{cut}}$, ranging $21 < [4.5] < 22.5$, and with different aperture radii, $0.5 < r < 2'$. As shown in Figure 8, richness increases with increasing magnitude cut adopted; this is not surprising since there are typically more

Table 2
SZE-selected Cluster Sample

Clus ID	R.A. (deg., J2000)	Decl. (deg., J2000)	NAME	z	$\log M_{500,SZ}$ (M_{\odot})	$\log R_{[4.5]}$ (galaxies Mpc^{-2})	N_{Cluster}	N_S
OBJ1	3.05417	16.0375	MOO J0012+1602 (1)	0.944	14.146 ^{+0.071} _{-0.085}	1.505 ^{+0.069} _{-0.082}	172	14.39
OBJ4	49.8517	-0.4225	MOO J0319-0025	1.194	14.491 ^{+0.027} _{-0.029}	0.902 ^{+0.126} _{-0.178}	104	12.19
OBJ5	153.535004	0.64056	MOO J1014+0038	1.27	14.531 ^{+0.025} _{-0.026}	1.423 ^{+0.075} _{-0.091}	165	13.49
OBJ7	228.677917	13.77528	MOO J1514+1346	1.059	14.342 ^{+0.055} _{-0.064}	1.501 ^{+0.069} _{-0.083}	176	14.02
OBJ8	216.637299	35.139889	IDCS J1426.5+3508 (2)	1.75	14.415 ^{+0.055} _{-0.063}	0.990 ^{+0.120} _{-0.166}	109	9.94
OBJ10	34.432999	-3.76	XLSSU J021744.1-034536 (3)	1.91	14.127 ^{+0.017} _{-0.018}	0.973 ^{+0.122} _{-0.171}	107	9.52
OBJ9	86.655128	-53.757099	SPT-CL J0546-5345 (4)	1.067	14.703 ^{+0.034} _{-0.037}	1.346 ^{+0.075} _{-0.091}	161	27.47
OBJ11	310.248322	-44.860229	SPT-CL J2040-4451	1.478	14.522 ^{+0.041} _{-0.045}	1.395 ^{+0.072} _{-0.087}	177	28.46
OBJ12	31.442823	-58.48521	SPT-CL J0205-5829	1.322	14.675 ^{+0.034} _{-0.037}	1.194 ^{+0.095} _{-0.122}	130	12.67
OBJ13	316.52063	-58.745075	SPT-CL J2106-5844	1.132	14.922 ^{+0.031} _{-0.033}	1.418 ^{+0.072} _{-0.086}	172	24.45
OBJ16	355.299103	-51.328072	SPT-CL J2341-5119	1.003	14.747 ^{+0.033} _{-0.036}	0.950 ^{+0.120} _{-0.166}	105	12.16
OBJ17	93.964989	-57.776272	SPT-CL J0615-5746	0.972	15.023 ^{+0.031} _{-0.033}	1.410 ^{+0.068} _{-0.081}	176	35.12
OBJ18	326.64624	-46.550034	SPT-CL J2146-4633	0.933	14.737 ^{+0.035} _{-0.038}	1.228 ^{+0.088} _{-0.110}	132	17.61
OBJ20	83.400879	-50.09008	SPT-CL J0533-5005	0.881	14.578 ^{+0.040} _{-0.044}	0.802 ^{+0.126} _{-0.179}	100	24.49
OBJ21	15.729427	-49.26107	SPT-CL J0102-4915	0.8701	15.159 ^{+0.030} _{-0.033}	1.496 ^{+0.071} _{-0.085}	162	10.60
OBJ22	9.175811	-44.184902	SPT-CL J0036-4411	0.869	14.512 ^{+0.047} _{-0.052}	1.414 ^{+0.077} _{-0.094}	147	10.13
OBJ23	72.27417	-49.024605	SPT-CL J0449-4901	0.792	14.69 ^{+0.036} _{-0.039}	1.384 ^{+0.076} _{-0.092}	146	17.81
OBJ24	359.922974	-50.164902	SPT-CL J2359-5009	0.775	14.557 ^{+0.041} _{-0.045}	1.013 ^{+0.114} _{-0.154}	104	11.54
OBJ25	353.105713	-53.967545	SPT-CL J2332-5358	0.402	14.723 ^{+0.036} _{-0.039}	1.291 ^{+0.083} _{-0.103}	105	12.88
OBJ26	325.139099	-57.457577	SPT-CL J2140-5727	0.4054	14.531 ^{+0.048} _{-0.054}	1.476 ^{+0.065} _{-0.077}	126	20.02
OBJ27	69.574867	-54.321243	SPT-CL J0438-5419	0.4214	15.033 ^{+0.031} _{-0.034}	1.582 ^{+0.061} _{-0.071}	137	17.77
OBJ28	87.904144	-57.155659	SPT-CL J0551-5709	0.423	14.696 ^{+0.037} _{-0.041}	1.626 ^{+0.054} _{-0.062}	154	28.82
OBJ29	62.815441	-48.321751	SPT-CL J0411-4819	0.4235	14.913 ^{+0.032} _{-0.035}	1.387 ^{+0.075} _{-0.091}	115	14.52
OBJ30	323.916351	-57.44091	SPT-CL J2135-5726	0.427	14.789 ^{+0.034} _{-0.037}	1.638 ^{+0.057} _{-0.065}	148	20.49
OBJ31	321.146179	-61.410179	SPT-CL J2124-6124	0.435	14.715 ^{+0.037} _{-0.040}	1.453 ^{+0.065} _{-0.077}	130	22.74
OBJ32	52.728668	-52.469772	SPT-CL J0330-5228	0.4417	14.824 ^{+0.034} _{-0.036}	1.570 ^{+0.064} _{-0.075}	134	13.24
OBJ33	77.337387	-53.705322	SPT-CL J0509-5342	0.4607	14.704 ^{+0.037} _{-0.040}	1.028 ^{+0.091} _{-0.116}	104	21.00
OBJ34	60.968086	-57.323669	SPT-CL J0403-5719	0.4664	14.574 ^{+0.044} _{-0.049}	1.475 ^{+0.069} _{-0.081}	129	15.99
OBJ35	103.962601	-52.567741	SPT-CL J0655-5234	0.4703	14.707 ^{+0.038} _{-0.042}	1.351 ^{+0.056} _{-0.065}	158	56.19
OBJ36	326.468201	-56.747559	SPT-CL J2145-5644	0.48	14.840 ^{+0.033} _{-0.036}	1.688 ^{+0.055} _{-0.063}	164	19.35
OBJ37	308.801147	-52.851883	SPT-CL J2035-5251	0.5279	14.793 ^{+0.035} _{-0.038}	1.741 ^{+0.050} _{-0.057}	194	29.60
OBJ38	354.352264	-59.704929	SPT-CL J2337-5942	0.775	14.926 ^{+0.031} _{-0.034}	1.402 ^{+0.076} _{-0.092}	144	14.14
OBJ39	82.019592	-53.002384	SPT-CL J0528-5300	0.7678	14.562 ^{+0.041} _{-0.046}	1.273 ^{+0.080} _{-0.098}	137	23.77
OBJ40	345.466888	-55.776756	SPT-CL J2301-5546	0.748	14.429 ^{+0.052} _{-0.060}	1.090 ^{+0.102} _{-0.133}	111	14.34
OBJ41	31.279436	-64.545746	SPT-CL J0205-6432	0.744	14.532 ^{+0.045} _{-0.050}	1.303 ^{+0.083} _{-0.103}	130	14.62
OBJ42	310.8284	-50.593838	SPT-CL J2043-5035	0.7234	14.656 ^{+0.040} _{-0.043}	1.474 ^{+0.066} _{-0.077}	165	27.70
OBJ43	314.217407	-54.993736	SPT-CL J2056-5459	0.718	14.545 ^{+0.043} _{-0.048}	1.491 ^{+0.065} _{-0.077}	165	25.30
OBJ44	315.093262	-45.805138	SPT-CL J2100-4548	0.7121	14.466 ^{+0.057} _{-0.066}	1.340 ^{+0.075} _{-0.091}	142	24.02
OBJ45	47.629108	-46.783417	SPT-CL J0310-4647	0.7093	14.635 ^{+0.040} _{-0.044}	1.091 ^{+0.105} _{-0.140}	107	11.51
OBJ46	19.598965	-51.943447	SPT-CL J0118-5156	0.705	14.575 ^{+0.044} _{-0.049}	1.449 ^{+0.074} _{-0.090}	143	11.00
OBJ47	0.249912	-57.806423	SPT-CL J0000-5748	0.7019	14.659 ^{+0.037} _{-0.040}	1.378 ^{+0.078} _{-0.096}	135	13.07
OBJ48	68.254105	-56.502499	SPT-CL J0433-5630	0.692	14.496 ^{+0.050} _{-0.056}	1.080 ^{+0.098} _{-0.127}	112	17.78
OBJ49	80.301186	-51.076565	SPT-CL J0521-5104	0.6755	14.614 ^{+0.039} _{-0.043}	1.494 ^{+0.066} _{-0.078}	159	22.39
OBJ50	38.255245	-58.327393	SPT-CL J0233-5819	0.663	14.594 ^{+0.041} _{-0.046}	1.391 ^{+0.077} _{-0.094}	134	13.00
OBJ51	33.106094	-46.950199	SPT-CL J0212-4657	0.6553	14.770 ^{+0.034} _{-0.038}	1.473 ^{+0.073} _{-0.087}	142	10.42
OBJ52	335.712189	-48.573456	SPT-CL J2222-4834	0.6521	14.734 ^{+0.036} _{-0.039}	1.477 ^{+0.070} _{-0.084}	147	15.01
OBJ53	77.920914	-51.904373	SPT-CL J0511-5154	0.645	14.611 ^{+0.040} _{-0.044}	1.376 ^{+0.074} _{-0.089}	139	21.06
OBJ54	85.716667	-41.004444	SPT-CL J0542-4100	0.642	14.713 ^{+0.038} _{-0.041}	1.405 ^{+0.069} _{-0.082}	148	26.83
OBJ55	40.861546	-59.512436	SPT-CL J0243-5930	0.6352	14.661 ^{+0.038} _{-0.042}	1.427 ^{+0.074} _{-0.090}	137	13.56
OBJ56	319.731659	-50.932484	SPT-CL J2118-5055	0.6254	14.557 ^{+0.047} _{-0.053}	1.301 ^{+0.078} _{-0.095}	130	21.38
OBJ57	326.531036	-48.780003	SPT-CL J2146-4846	0.623	14.592 ^{+0.044} _{-0.049}	1.585 ^{+0.062} _{-0.072}	165	17.95
OBJ58	89.925095	-52.826031	SPT-CL J0559-5249	0.609	14.762 ^{+0.034} _{-0.037}	1.349 ^{+0.070} _{-0.083}	143	30.61
OBJ59	314.587891	-56.14529	SPT-CL J2058-5608	0.606	14.468 ^{+0.053} _{-0.060}	1.294 ^{+0.076} _{-0.092}	132	25.23
OBJ60	326.69574	-57.614769	SPT-CL J2146-5736	0.6022	14.570 ^{+0.043} _{-0.047}	1.417 ^{+0.072} _{-0.086}	139	19.48
OBJ61	356.184692	-42.720924	SPT-CL J2344-4243	0.596	15.081 ^{+0.031} _{-0.033}	1.625 ^{+0.062} _{-0.072}	162	10.91
OBJ62	64.345047	-47.813923	SPT-CL J0417-4748	0.581	14.870 ^{+0.033} _{-0.035}	1.258 ^{+0.086} _{-0.107}	117	14.87
OBJ63	83.608215	-59.625652	SPT-CL J0534-5937	0.5761	14.439 ^{+0.055} _{-0.064}	1.223 ^{+0.079} _{-0.096}	125	25.93

Table 2
(Continued)

Clus ID	R.A. (deg., J2000)	Decl. (deg., J2000)	NAME	z	$\log M_{500,SZ}$ (M_{\odot})	$\log R_{[4.5]}$ (galaxies Mpc^{-2})	N_{Cluster}	N_S
OBJ64	352.960846	-50.863926	SPT-CL J2331-5051	0.576	$14.748^{+0.034}_{-0.037}$	$1.256^{+0.088}_{-0.111}$	114	12.34
OBJ65	327.181213	-61.277969	SPT-CL J2148-6116	0.571	$14.649^{+0.039}_{-0.043}$	$1.473^{+0.067}_{-0.080}$	144	20.27
OBJ66	74.116264	-51.27684	SPT-CL J0456-5116	0.5615	$14.707^{+0.036}_{-0.040}$	$1.450^{+0.069}_{-0.083}$	139	19.00
OBJ67	38.187614	-52.957821	SPT-CL J0232-5257	0.5559	$14.729^{+0.036}_{-0.040}$	$1.432^{+0.075}_{-0.090}$	129	11.75
OBJ68	305.027344	-63.243397	SPT-CL J2020-6314	0.5361	$14.515^{+0.048}_{-0.054}$	$1.306^{+0.069}_{-0.082}$	137	33.81
OBJ69	304.483551	-62.978218	SPT-CL J2017-6258	0.5346	$14.587^{+0.042}_{-0.047}$	$1.359^{+0.066}_{-0.078}$	142	34.27
OBJ70	346.729767	-65.091042	SPT-CL J2306-6505	0.5298	$14.758^{+0.036}_{-0.039}$	$1.742^{+0.053}_{-0.060}$	182	16.94
OBJ71	56.724724	-54.650532	SPT-CL J0346-5439	0.5297	$14.738^{+0.036}_{-0.039}$	$1.541^{+0.066}_{-0.077}$	143	14.41
26	4.640833	16.438056	MACS J0018.5+1626 (5)	0.5456	$14.938^{+0.040}_{-0.044}$	$1.645^{+0.061}_{-0.071}$	162	14.31
355	73.54625	-3.015	MACS J0454.1-0300 (5)	0.5377	$14.858^{+0.054}_{-0.061}$	$1.676^{+0.059}_{-0.068}$	178	25.66
621	149.012083	41.118889	400d J0956+4107 (5)	0.587	$14.844^{+0.049}_{-0.055}$	$1.322^{+0.086}_{-0.107}$	118	9.89
1050	206.875	-11.748889	RXC J1347.5-1144 (5)	0.4516	$15.026^{+0.029}_{-0.031}$	$1.726^{+0.056}_{-0.064}$	162	15.81

Note. $M_{500,SZ}$ values as reported by (1) Brodwin et al. (2015), (2) Brodwin et al. (2012), (3) Mantz et al. (2014), (4) Bleem et al. (2015), (5) Planck Collaboration et al. (2015).**Figure 8.** Dependence of average richness, $\langle R_{[4.5]} \rangle$, with adopted $4.5 \mu\text{m}$ magnitude cuts, $[4.5]_{\text{cut}}$, and aperture radii for the reference X-ray “deep sample.” Error bars indicate the standard deviation of the mean.

galaxies at fainter luminosities for a canonical luminosity function. This test validates the importance of adopting a uniform magnitude cut while dealing with a heterogeneous, archival sample. We also note that the slope and standard deviation of richness is much smaller for the larger, adopted 2 arcmin radius aperture than for the smaller apertures. For the adopted 2 arcmin aperture radius, the dependence of the mean richness, $\langle R_{[4.5]} \rangle$, with the magnitude cut adopted, $[4.5]_{\text{cut}}$, is best fitted with the linear relation

$$\frac{\langle R_{[4.5]} \rangle}{\text{galaxies Mpc}^{-2}} = (-358.71) + (18.97) \times \frac{[4.5]_{\text{cut}}}{\text{AB mag}}. \quad (3)$$

This relation allows us to quantify the expected increase in average richness value at increasing depths of the observations due simply to an intrinsic photometric effect, not due to

cluster-to-cluster variations or dynamical state. By means of extrapolation, this relation could be also used to predict the expected average richness value for samples of clusters at similar redshifts with upcoming, wide-area, infrared surveys (see discussion in Section 6.4).

5. Calibrating a Cluster Mass–Richness Relation at $0.4 < z < 2.0$

In this section, we calibrate mass–richness relations based on our richness estimates defined in Section 4 and on total cluster masses as described in Sections 2.1 and 2.2. In Figure 9, we show the relations we find for the 47 clusters of the X-ray sample (top panel) and the 69 clusters of the SZE sample (bottom panel). We perform a weighted linear least squares fit of the data for each sample individually with a single linear relation on log quantities, where errors in both variables are also taken into account (Press et al. 2002, Section 15.6), and find

$$\log \frac{M_{500,X}}{M_{\odot}} = (13.68 \pm 0.17) + (0.57 \pm 0.23) \cdot \log \frac{R_{[4.5]}}{\text{gals Mpc}^{-2}}, \quad (4)$$

and

$$\log \frac{M_{500,SZ}}{M_{\odot}} = (13.34 \pm 0.21) + (0.93 \pm 0.22) \cdot \log \frac{R_{[4.5]}}{\text{gals Mpc}^{-2}}. \quad (5)$$

In Figure 10, we show the relation we find for the 116 clusters of the combined sample (solid black line):

$$\log \frac{M_{500}}{M_{\odot}} = (13.56 \pm 0.25) + (0.74 \pm 0.18) \cdot \log \frac{R_{[4.5]}}{\text{gals Mpc}^{-2}}. \quad (6)$$

To test the robustness of our fit, we have also run a bootstrap Monte Carlo test, in which the mass–richness relation is repeatedly resampled to reveal whether or not a small sample of

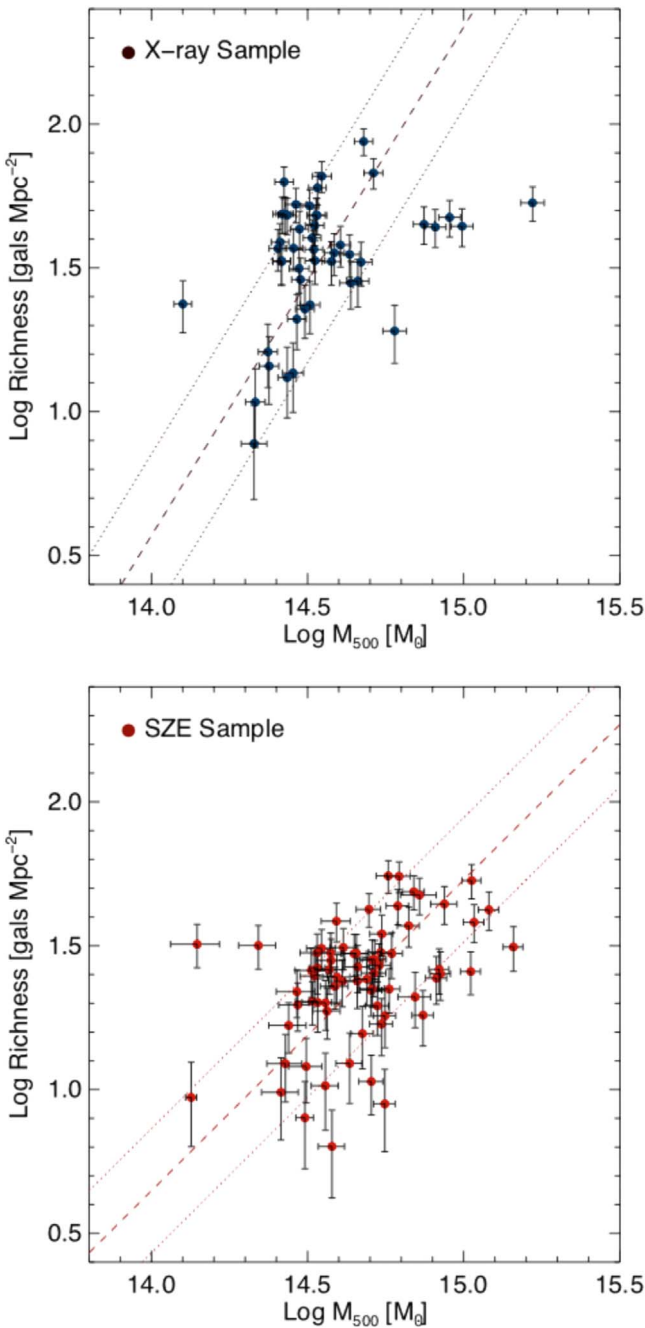


Figure 9. $4.5 \mu\text{m}$ richness–mass relation for a sample of 47 X-ray selected clusters (top panel) and 69 SZE-selected clusters (bottom panel) at $0.4 < z < 2.0$. The dashed lines correspond to the best straight-line fits to data with errors in both coordinates for each sample respectively. The dotted lines indicate the 68.3% confidence regions of each fit.

clusters could, for instance, dramatically alter the result of the fit. We run the least-square fitting algorithm 1000 times and at each repetition we randomly toss out 25% of the sample. We then infer the mean and standard deviation of the intercept and slope distribution for the 1000 fit results. We find the latter values in perfect agreement with the ones of Equation (6).

We have also checked whether a small subsample of high-mass clusters could largely alter the result of the fit. However, even excluding the three most massive clusters in the sample, the resulting values of intercept and slope and their errors are still consistent within 1σ of the ones presented in Equation (6).

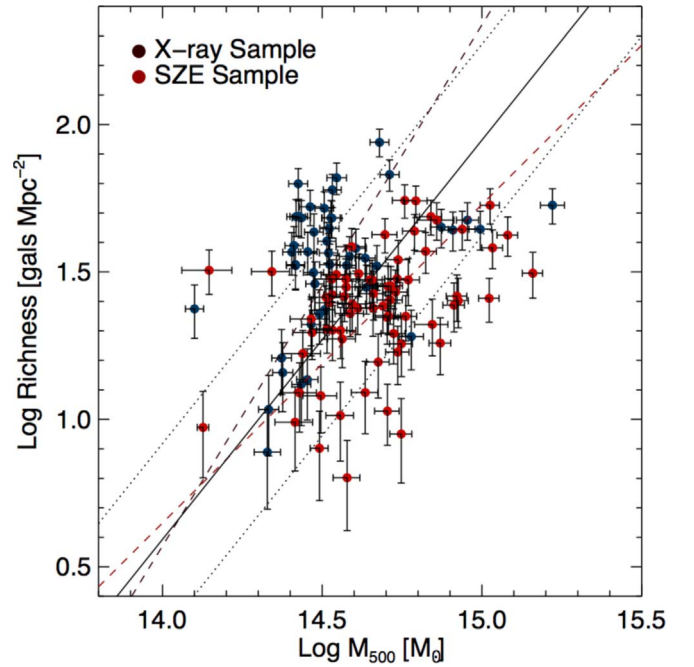


Figure 10. $4.5 \mu\text{m}$ richness–mass relation for a sample of 47 X-ray selected clusters (blue circles) and 69 SZE-selected clusters (red circles) at $0.4 < z < 2.0$. The blue and red dashed lines correspond to the best straight-line fits to the individual samples shown previously in Figure 9. The solid line indicates the fit to the combined sample and the dotted lines indicate the 68.3% confidence regions of this fit.

Based on the 68.3% confidence regions of the fits (dotted lines), we estimate the associated errors in mass at fixed richness to be ± 0.25 dex. We will discuss the dependence of the scatter of this relation with concentration in Section 6.2. The intrinsic scatter of the relation is measured in the $R_{[4.5]}$ direction around the best-fitting $R_{[4.5]}-M$ relation for that sample via bootstrapping method (Tremaine et al. 2002; Kelly 2007; Andreon & Hurn 2013) and is denoted as $\sigma_{R_{[4.5]}|M}$. We find $\sigma_{R_{[4.5]}|M} = 0.32$ dex for our sample.

We compare the measured scatter in our relation with literature richness and mass estimates. Using an r -band luminosity-based optical richness estimator, R_L ; Planck Collaboration et al. (2014) found the associated error in mass at fixed richness to be ± 0.27 dex. The intrinsic scatter of their R_L-M relation, $\sigma_{R_L|M} = 0.35$, is also similar to the value that we have found. Note that R_L was defined by Wen et al. (2012) for a large sample of low-redshift Sloan Digital Sky Survey (SDSS, York et al. 2000) selected clusters for which X-ray masses were provided by Piffaretti et al. (2011). We note that their method cannot be extended to all clusters in our sample because SDSS lacks coverage of the southern sky and because deeper optical data than the one available from SDSS would be required to detect the bulk of cluster galaxies at $0.6 < z \lesssim 2$.

Also at lower redshifts, $0.03 < z < 0.55$, Andreon & Hurn (2010) and Andreon (2015) used multiband SDSS photometry to define an optical richness estimator, n_{200} , aimed at counting red cluster members within a specified luminosity range and color as a proxy of the total mass, M_{200} , within the R_{200} radius. These predicted masses are found to have a smaller 0.16 dex scatter with mass, but require optical photometry in at least two bands.

As a comparison with other observable-mass scaling relations, we note that Maughan (2007) studied the L_X-M relation for

a sample of 115 clusters at $0 < z < 1.3$ and found the associated error in mass at fixed luminosity to be ± 0.21 dex. They measured the intrinsic scatter in the L_X - M relation to be $\sigma_{L|M} = 0.39$ when all of the core emission is included in their L_X measurements. Interestingly, they have also demonstrated that the scatter can greatly be reduced to $\sigma_{L|M} = 0.17$ by excising the core emission in their L_X measurements. Furthermore, Rozo et al. (2014a, 2014b) used SZE data from *Planck* and X-ray data from *Chandra* and *XMM-Newton* to calibrate Y_X - M , Y_{SZ} - Y_X and Y_{SZ} - M relations for different samples of clusters at $z < 0.3$. They found low values for the scatters of the Y_{SZ} - M relations, $\sigma_{Y_{SZ}|M} = 0.12$ – 0.20 .

To summarize, the method we have proposed here requires only shallow, single pointing, single band observations and an estimate of the cluster center position and redshift to provide reliable richness-based cluster mass estimates. The very low observational cost associated with our approach makes it potentially available for very large samples of clusters at $0.4 < z < 2.0$.

6. Discussion

In this section, we discuss the richness distribution and galaxy surface density profile for our samples. We also examine potential sources of the scatter in the mass–richness relation, including sample selection and galaxy concentration. We then explore the possibility of extending our method to other MIR all-sky surveys like *WISE*, and the implications of our findings on future, wide-field near-infrared cluster surveys like *Euclid*.

6.1. Richness Distribution and Profiles

In the top panel of Figure 11 we show the distributions of richness for our samples. The X-ray sample (blue histogram and blue dashed line) shows larger median richness values than the SZ sample (red histogram and red dashed line). This difference is statistically significant, as shown by the Kolmogorov–Smirnov (KS) test, which provides a probability $P_{KS} \sim 10^{-6}$ that the observed distributions of richness are extracted from the same parent population.

As the SZE sample probes the redshift range $z > 1$ more extensively, we tested whether this difference in median richness could depend on the relative redshift distribution of the two samples. Hence we performed the KS test again only for clusters in the redshift range $0.4 < z < 0.8$, which is well sampled by both methods. However, the latter test produces a similar outcome of the former, ruling out this possibility.

In the bottom panel of Figure 11 we show the dependence of richness on aperture radius for both cluster samples. We divide each sample in two equally populated bins of X-ray or SZE derived cluster masses. We calculate the richness profiles by measuring the background-subtracted projected surface density of galaxies with $[4.5] < 21$ AB within $r = 30''$, $60''$, $120''$ from the cluster center. We find the shapes of the richness profiles to be similar for both samples and in each mass bins and the richness values consistent within the large scatter. However, the low-mass X-ray sample appears to be as rich as the high-mass SZ sample. Hence at fixed cluster mass, X-ray clusters appear to have, on average, higher near-infrared richness than SZ-selected clusters.

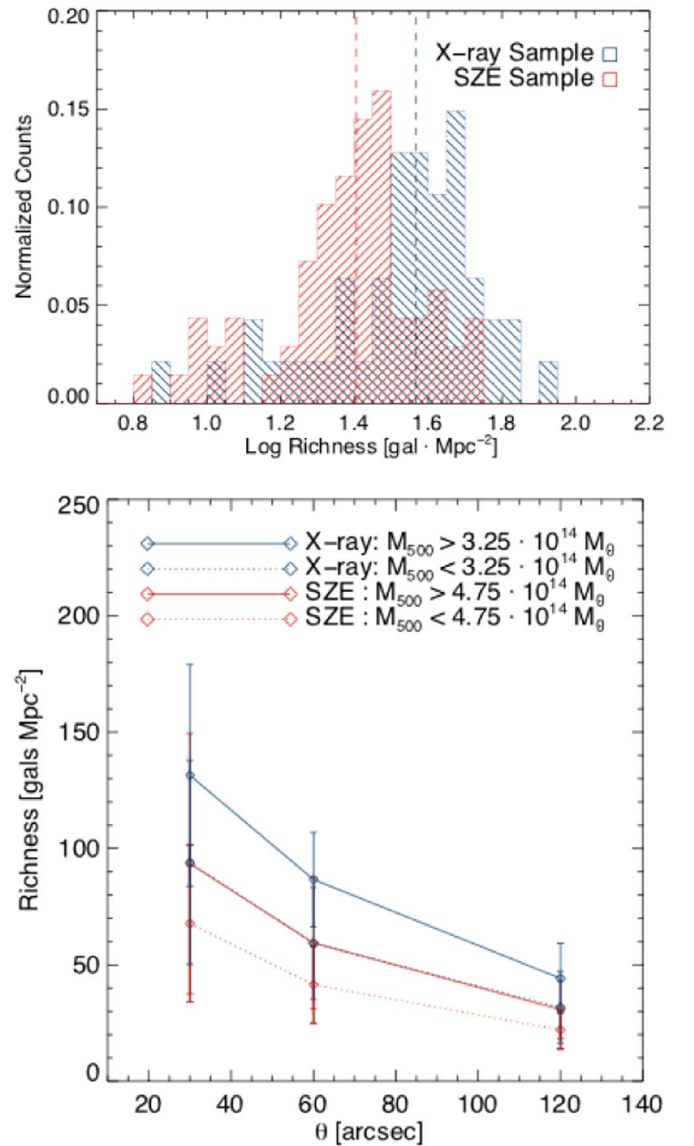


Figure 11. Top: histogram of richness of the X-ray (blue) and the SZE (red) samples. The dashed lines indicate the median richness of each sample. Bottom: dependence of richness with cluster mass and aperture radius for the X-ray (blue) and the SZE (red) samples.

One possibility is that this difference is due to systematics in derived masses for the X-ray and SZ samples. For example, if, despite the careful re-calibration in Section 2, the X-ray masses are underestimates, then the higher richness of the X-ray clusters would imply that they are more massive clusters. Given the extensive work on calibrating X-ray and SZ observables with mass, this seems unlikely. Yet, without having a statistically significant SZ, X-ray, and richness estimates sample of the same clusters in this redshift range, we cannot definitively rule it out.

Alternately, could this be due to a selection effect, where the X-ray surveys, at a fixed cluster mass, typically select richer systems where galaxy merging has been, on average, less effective than in SZE-selected clusters? X-ray surveys are indeed usually considered biased toward selecting more relaxed, more evolved systems (e.g., Eckert et al. 2011). This is because of the presence of a surface brightness peak in the so-called “cool core” clusters. The clear peak of X-ray emission

is more easily detected in the wide shallow surveys of *ROSAT*, for instance, and it is considered to be associated with a decrease in the gas temperature, typical of relaxed structures.

On the other hand, most of the clusters newly discovered by *Planck* via SZE show clear indication of morphological disturbances in their X-ray images, suggesting a more active dynamical state (Planck Collaboration et al. 2011). Interestingly, Rossetti et al. (2016), measuring the offset between the X-ray peak and the BCG population, a known indicator of an active cluster dynamical state (e.g., Sanderson et al. 2009; Mann & Ebeling 2012), found evidence of the dynamical state of SZ-selected clusters to be significantly different from X-ray-selected samples, with a higher fraction of non-relaxed, merging systems.

In the hierarchical cluster formation scenario, clusters form by the infall of less massive groups along the filaments. Therefore while it is possible that a larger fraction of SZ-selected clusters in our sample are in a less developed stage of cluster formation, if the difference in richness between our samples was to be explained with the fact that X-ray clusters were more evolved and had accreted more galaxies within R_{500} , then they should also be the most massive. This has, however, not been found, as clearly shown in Figure 3, unless there are mass calibration uncertainties larger than those discussed.

An intriguing possibility is that there are differences in the intrinsic baryon fraction within R_{500} relative to the cosmological baryon fraction between the cluster samples. If X-ray clusters at these redshifts harbor a larger baryon fraction per unit dark-matter halo mass compared to SZE cluster samples within the aperture radius, it could account for lower total masses, more efficient cooling of the intracluster medium by thermal Bremsstrahlung, and the resultant increased star-formation efficiency could result in a larger population of luminous galaxies translating to a higher richness. Indeed, simulations like the millennium simulations show a factor of two variation in the baryon fraction of $>10^{14} M_{\odot}$ dark-matter halos, which could easily account for both the differences in derived masses and richness values. Even among the X-ray cluster sample, Vikhlinin et al. (2009) showed that the baryon fraction increases with increasing mass among which there is likely the origin of a richness–mass correlation that we derive. A comparison between the density profiles of SZ clusters and X-ray clusters in Planck Collaboration et al. (2011) shows that SZ clusters show shallower density profiles than X-ray-selected clusters, which may again argue that the baryons in SZE-selected clusters are predominantly at larger radii than in the X-ray sample. However, extracting effects such as these from the data would again require SZ, X-ray, and richness estimates of the same clusters in this redshift range while our study has rather heterogeneous samples with different origins that we have attempted to place on the same calibration scale. Apart from stating these possibilities, it is challenging for us to definitively claim one of them as an origin for the observed difference.

6.2. Galaxy Concentration

In an attempt to understand the source of the scatter in the mass–richness relation, we also measure the galaxy concentration of our cluster samples, defined as the ratio between the richness measured within $r = 60''$ and $r = 120''$. By definition, a higher value of galaxy concentration corresponds to systems with a steeper galaxy surface density profile. As shown in

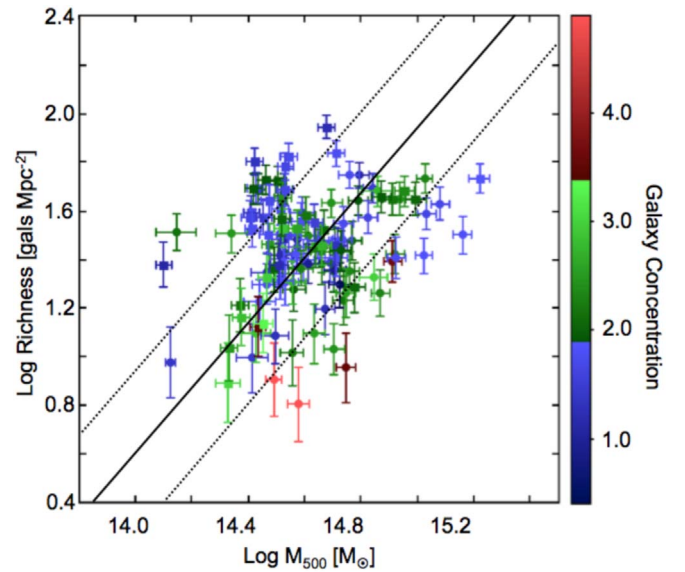


Figure 12. $4.5 \mu\text{m}$ richness vs. mass relation color-coded by galaxy concentration for the combined sample. The solid line indicates the linear fit to the sample where errors in both variables are taken into account. The dotted lines indicate the 68.3% confidence regions of this fit.

Figure 12, there is a hint that clusters that deviate the most from the fitted mass–richness relation are also the ones with the most centrally concentrated galaxy surface density profile. If we include a correction for galaxy concentration, the scatter of the mass–richness relation slightly decreases so that the associated error in mass at fixed richness is found to be ± 0.22 dex, indicating that surface density concentration does play a significant role in the scatter.

Possible origins for this are blending and source confusion in the IRAC image, beam dilution when the $2'$ aperture is much larger than the cluster overdensity, or the impact of galaxy merging on richness estimates. Images of galaxy clusters that are more centrally concentrated are more likely to be affected by the blending of some cluster galaxies in the core, given the *Spitzer* angular resolution. This could result in underestimating their richness. The amount of confusion is linearly proportional to the surface density of galaxies. A cluster that is four times as concentrated in surface density would have its richness underestimated by 0.6 dex, which is the amount of offset of the red points in Figure 12 from the best-fit line.

Alternatively, systems with higher central galaxy concentrations have their richness estimate, calculated within a radius $r = 120''$, biased by the fact that the aperture chosen is too large, hence their richness is relatively smaller compared to less centrally concentrated systems. However, if this was purely an observational bias, we should have found a correlation between galaxy concentration and θ_{500} derived for the hot gas in the intracluster medium, a proxy of cluster size, which is not apparent.

If mergers were responsible for the scatter in the richness–mass relation, clusters of the same total mass that might have experienced more or less merger events in their cores with respect to their outskirts would result in lower or higher concentration measurements and would therefore be found to have lower or higher values of richness. In the most extreme cases, as shown in Figure 13, galaxy clusters of the same total mass (as probed by their gas) and at the same lookback time may have experienced very different evolutionary processes,

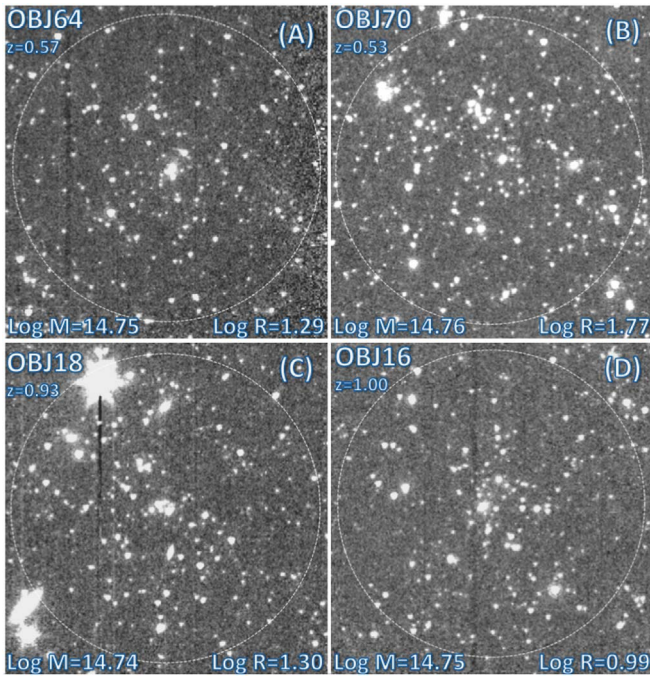


Figure 13. *Spitzer*/IRAC images of four clusters in our sample with similar $M_{500,SZ}$ but with different richness or redshifts measured. The white dashed circles have a radius $r = 2'$, centered on the reported cluster. Images (A) and (B) show clusters at similar redshift, $z \sim 0.5$, while (C) and (D) are instead at $z \sim 1$. Despite having similar redshifts and masses, (A) and (B) are found with large differences in their richness values suggesting that there may be other dependencies. Images (A) and (C), however, show clusters of the same mass, found with a similar richness despite being at different redshift.

resulting in large differences in richness and concentration inferred from the number and location of their cluster members.

Thus we conclude that the scatter we derive in the richness–mass relation is likely due to a combination of source confusion and differences in evolutionary history of the clusters.

6.3. WISE 4.5 μm Richness

The AllWISE⁸ program combined data from the cryogenic *Wide-field Infrared Survey Explorer* mission (*WISE*, Wright et al. 2010) and the NEOWISE (Mainzer et al. 2011) post-cryogenic survey to deliver a survey of the full MIR sky. Since all-sky catalogs in the W2 band at 4.6 μm are available, it could allow us to potentially extend our method outside the *Spitzer* footprint. Therefore in this section we test whether our proposed method of deriving MIR richness estimates can be applied robustly to the publicly available *WISE* data.

To this aim, we use archival *WISE* 4.6 μm data available at the location of all our clusters and apply the same method described in Section 4. The SEIP source list contains W2 photometry for positional counterparts found in the AllWISE release both for all clusters in our sample and for the control SpUDS field. In Figure 14 (left panel), we show the richness estimates based on data from *Spitzer* and *WISE* for our SZE sample. The dashed lines indicate the straight-line fit to be compared to the 1:1 (solid) line. We note that there are several catastrophic outliers and that *Spitzer*-based richness values are systematically higher than the *WISE*-based counterparts. We note that *WISE* is less sensitive than *Spitzer* and that its angular resolution is also poorer (6''4 versus 2''0).

⁸ <http://wise2.ipac.caltech.edu/docs/release/allwise/>

To test whether the catastrophic discrepancies in the *Spitzer* versus *WISE* richness estimates could be ascribed to confusion, we sum the flux densities of every object detected within $r = 120''$ from each cluster center by the two instruments. We also subtract a median flux density from the background field to get a flux overdensity at the location of the cluster. Source confusion makes groups of sources in a high resolution image appear as a single bright source in a low-resolution image. By adding the flux densities we take out the effect of confusion, which would bias low richness estimates. We then use the redshift of the cluster to translate the summed flux overdensity to a luminosity surface density. As shown in the right panel of Figure 14, we find that the total luminosity densities for each cluster appear to be conserved, as the two instruments provide matching measurements. Therefore we can ascribe the aforementioned discrepancies solely to the poorer angular resolution of *WISE*, with richness estimates highly depending on the particular projected cluster galaxy geometry. At the *WISE* image quality, we expect a higher number of sources to be blended, resulting in lower counts of galaxies per cluster, yielding lower richness values than those measured by *Spitzer*. For example, source overdensities of 30 galaxies in the $2'$ radius aperture would correspond to 10 gals Mpc^{-2} , which in turn would correspond to a ratio of 11 for the number of *WISE* beams per source. This is well below the classical confusion limit. In reality, the confusion is even higher since the average underlying foreground source density would also contribute to confusion noise.

To summarize, we deem *WISE*-based richness estimates to be poorer proxies for cluster mass preventing us from effectively extending our method beyond the *Spitzer* footprint. Calibrating a mass–richness relation for the *WISE* data set will require a different technique and is therefore beyond the scope of this paper.

6.4. Future Wide-field Near-infrared Cluster Surveys

The upcoming *Euclid* and *WFIRST* missions aim to survey large portions of the extragalactic sky in the near infrared (e.g., H band) to measure the effects of dark energy, but also have distant cluster studies as a key scientific goal. The *Euclid* wide-area survey, in particular, will observe 15,000 deg^2 , almost the entire extragalactic celestial sphere, down to a 5σ point-source depth of $H = 24$ mag (AB). They plan to use photometric redshift overdensities to identify clusters but that requires ancillary ground-based optical data which is currently being taken. In this section, based on the results of our analysis, we try to provide a simple prediction of the expected richness values for *Euclid*-selected clusters and the range of masses that will be accessible.

Euclid is expected to detect $\sim 2 \times 10^6$ clusters at all redshifts, with $\sim 4 \times 10^4$ of them at $1 < z < 2$ with cluster masses $M_{200} \gtrsim 8 \times 10^{13} M_{\odot}$ (Sartoris et al. 2016; Ascaso et al. 2017). The cluster sample in our study spans a similar mass and redshift range, hence we can attempt to predict the average richness expected for clusters at $0.4 < z < 2.0$ as a function of mass in the *Euclid* survey.

In Figure 7, we show the evolution of the [3.6]–[4.5] (left panel) and $H - [4.5]$ color (middle panel) with redshift for a set of Bruzual & Charlot (2003) stellar population models with exponentially declining star-formation rates. We show both the typical color evolution expected for an early-type galaxy (assuming $\tau = 0.1$ Gyr) and a star-forming galaxy

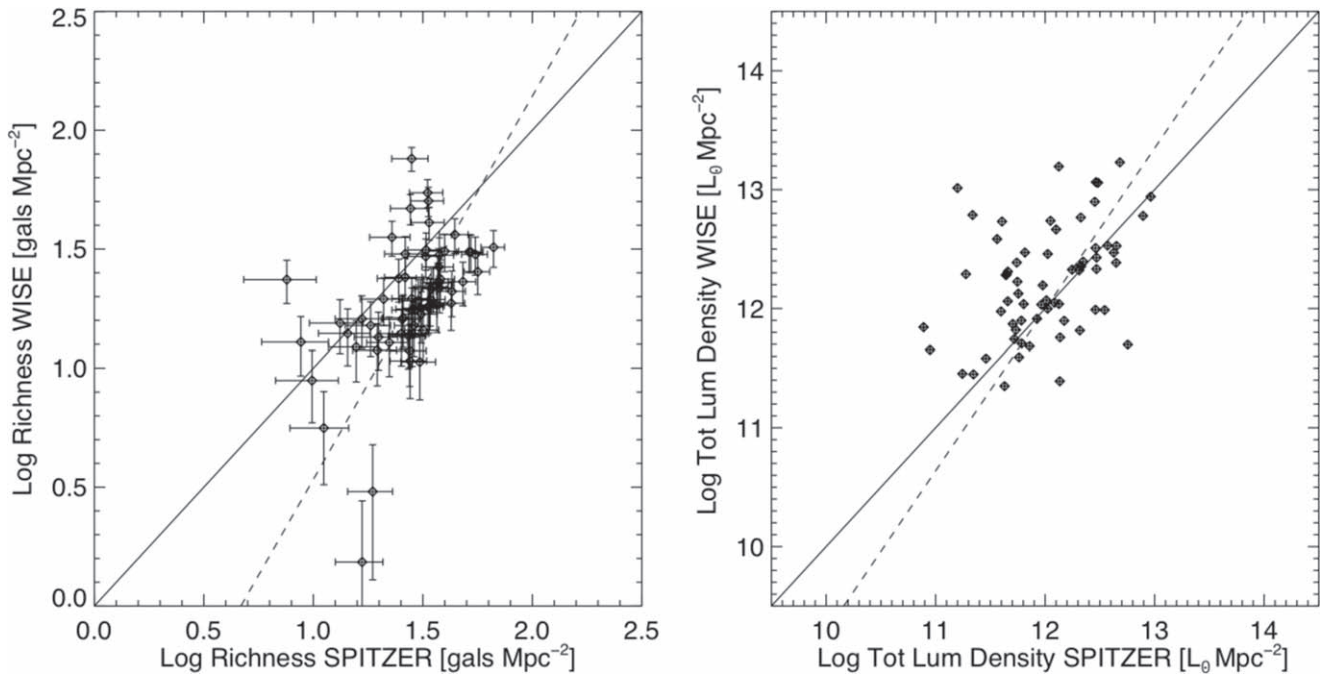


Figure 14. Comparison of richness estimates (left panel) and total luminosity density of all sources measured within $r = 120''$ from each cluster center (right panel) based on data from *Spitzer* at $4.5 \mu\text{m}$ and *WISE* at $4.6 \mu\text{m}$. The solid lines represent the identity (1:1) lines. The dashed lines correspond to the best straight-line fit to the data with errors in both coordinates.

($\tau = 1.0$ Gyr) as described in Rettura et al. (2010, 2011). As noted by several authors (e.g., Papovich 2008; Muzzin et al. 2013; Wylezalek et al. 2013; Rettura et al. 2014), the [3.6]–[4.5] color is fairly insensitive to different modes of star formation out to $z \sim 3$ and can be used as a good redshift indicator at $z > 1.3$. The $H - [4.5]$ color, instead, is more sensitive to galaxy star-formation history, in particular between $1 < z < 2$.

According to the models shown in the middle panel of Figure 7, we expect the $H - [4.5]$ color of a galaxy to vary between -0.7 and 0.75 AB (dashed lines) depending on its type at $0.4 < z < 2.0$ (gray shaded area). This would imply that to match the *Euclid* $H_{\text{cut}} = 24$ AB depth, we need an equivalent *Spitzer* $4.5 \mu\text{m}$ survey to reach $[4.5]_{\text{cut}} = 24.7$ AB.

In Section 4.1, based on our “deep” subsample of 36 clusters for which the deepest IRAC coverage was available in the *Spitzer* archive, we derived a relation between the survey depth and the average richness of our cluster sample. As we have demonstrated, we are already below the knee of the galaxy luminosity function at these redshifts and we do not expect the slope of the relation to change as we go deeper. Using Equation (3), we can then predict the richness of clusters at an equivalent depth of $[4.5]_{\text{cut}} = 24.7$, i.e., down to $H_{\text{cut}} = 24$. We predict the following levels of richness (in galaxies Mpc^{-2}) for *Euclid*-detected clusters as a function of cluster mass: $\log R_{[H]} = 1.78 \pm 0.26$ ($\log M_{500} < 14.5$), $\log R_{[H]} = 1.87 \pm 0.21$ ($14.5 \leq \log M_{500} \leq 14.75$), and $\log R_{[H]} = 1.99 \pm 0.16$ ($\log M_{500} > 14.75$). In the right panel of Figure 7 we show the expected mean richness (and standard deviation of the mean) in bins of cluster mass for the *Euclid* clusters at $0.4 < z < 2.0$, propagating the uncertainty in the fit required to extrapolate to these faint flux densities. For immediate comparison with the future observational data, the figure reports the expected richness values in units of galaxies arcmin^{-2} . We

conclude that typical *Euclid* clusters that are about $3 \times 10^{14} M_{\odot}$ will show galaxy overdensities of ~ 12 galaxies arcmin^{-2} .

7. Summary

In this paper we have studied a sample of 116 X-ray and SZE-selected galaxy clusters at $0.4 < z < 2.0$ observed by *Spitzer* at $4.5 \mu\text{m}$. Together, they span more than a decade in total cluster mass. With the aim of providing a simple and efficient observable that easily translates as a proxy for cluster mass, we have defined a $4.5 \mu\text{m}$ richness parameter that requires just a single pointing of IRAC imaging and shallow observing time (~ 90 s) that reaches a depth of $[4.5] < 21$ AB mag. Our results are as follows.

1. We have derived *ROSAT*-based X-ray bolometric luminosities and masses that are in agreement with independent studies performed using *Chandra* data by Maughan (2007) and Maughan et al. (2012).
2. By analyzing deeper IRAC imaging data, available for a subsample of systems, we have studied and parameterized the dependence of our richness parameter on survey depth and aperture radius. We have found that richness measured in the larger radius adopted here, $r = 2'$, is less sensitive to variations in depth.
3. We have calibrated a mass–richness relation for both subsamples individually and combined. We have fitted linear relations in log–log space and estimated the associated error in mass at fixed richness to be ± 0.17 , 0.22 , 0.25 dex for the X-ray, SZE, and the combined samples, respectively. We find a slight dependence of the scatter with galaxy concentration, defined as the ratio between richness measured within an aperture of 1 and 2 arcmin.

4. We have measured the intrinsic log scatter of our $4.5 \mu\text{m}$ richness–mass relation for our combined sample, $\sigma_{R_{4.5}|M} = 0.32$ dex. The value of scatter we found is similar to the one obtained by the Planck Collaboration et al. (2014) adopting deeper SDSS-based optical richness estimator at lower redshifts. We note that our richness estimates do not require an IRAC color selection and that we do not rely on time-consuming optical imaging data. The scatter associated with our observable is larger than the one obtained by Andreon (2015) and Rozo et al. (2014b) that have adopted richness estimates that require deeper multiband observations, which are time consuming, particularly at high redshifts.
5. We have found that similar *WISE*-based $4.6 \mu\text{m}$ richness estimates would provide poorer proxies of cluster mass due to the lower angular resolution of the data with respect to *Spitzer*/IRAC, which results in source confusion.
6. Finally, we provide a calibration of the average richness as a function of cluster mass in the near infrared, which can be applied to galaxy overdensities that will be detected by the upcoming *Euclid* mission through its wide-area near-infrared survey.

As *Spitzer* continues to survey large area of the sky during its extended *Warm Mission*, our current results make already simple richness-based cluster mass estimates available for large samples of clusters at a very low observational cost up to $z \sim 2$.

As more clusters will be discovered at $z > 1.3$ by ongoing and upcoming large X-ray, SZE, optical, and infrared survey (e.g., *eRosita*, SPTpol, SPT3G, DES, *Euclid*), we expect to be able to soon expand our calibration sample. The new data will enable a more in-depth study focused on the adoption of a physical distance aperture and on the introduction of a color cut to further improve the reliability of our richness estimator as a mass proxy.

A.R. is grateful to the *Spitzer* Archival Team for providing access to advanced data products and is thankful to Dr. Peter Capak for providing access to the SEIP photometry pipeline. A.R. is grateful to Drs. M. Nonino, L. Girardi for discussions and providing access to the TRILEGAL model runs. A.R. is grateful to Drs. Mark Brodwin, Anthony Gonzalez, Ben Maughan, Adam Mantz, Mauro Sereno, Veronica Strazzullo, and Loredana Vetere for interesting discussions, comments, and suggestions that improved this manuscript. This work is based on data obtained with the *Spitzer Space Telescope*, which is operated by the Jet Propulsion Lab (JPL), California Institute of Technology (Caltech), under a contract with NASA. Support was provided by NASA through contract number 1439211 and 1484822 issued by JPL/Caltech.

aastex-help@aaas.org.

Facilities: *Spitzer*, *WISE*, *IRSA*, *ROSAT*, *CXO*, *XMM*, *SPT*, *Planck*, *CARMA*.

ORCID iDs

A. Rettura  <https://orcid.org/0000-0002-5615-256X>

R. Chary  <https://orcid.org/0000-0001-7583-0621>

References

- Abell, G. O. 1958, *ApJS*, 3, 211
- Allen, S. W., Evrard, A. E., & Mantz, A. B. 2011, *ARA&A*, 49, 409
- Andreon, S. 2006, *A&A*, 448, 447
- Andreon, S. 2013, *A&A*, 554, A79
- Andreon, S. 2015, *A&A*, 582, A100
- Andreon, S. 2016, *A&A*, 587, A158
- Andreon, S., & Congdon, P. 2014, *A&A*, 568, A23
- Andreon, S., & Hurn, M. 2013, *Stat. Anal. Data Min.: ASA Data Sci. J.*, 6, 15
- Andreon, S., & Hurn, M. A. 2010, *MNRAS*, 404, 1922
- Andreon, S., Serra, A. L., Moretti, A., & Trinchieri, G. 2016, *A&A*, 585, A147
- Arnaud, K. A. 1996, in ASP Conf. Ser. 101, *Astronomical Data Analysis Software and Systems V*, ed. G. H. Jacoby & J. Barnes (San Francisco, CA: ASP), 17
- Ascaso, B., Mei, S., Bartlett, J. G., & Benítez, N. 2017, *MNRAS*, 464, 2270
- Ascaso, B., Wittman, D., & Dawson, W. 2014, *MNRAS*, 439, 1980
- Ashby, M. L. N., Stern, D., Brodwin, M., et al. 2009, *ApJ*, 701, 428
- Austermann, J. E., Aird, K. A., Beall, J. A., et al. 2012, *Proc. SPIE*, 8452, 84521E
- Bahcall, N. A., & Cen, R. 1993, *ApJL*, 407, L49
- Bartelmann, M., & Schneider, P. 2001, *PhR*, 340, 291
- Bartlett, J. G., & Silk, J. 1994, *ApJ*, 423, 12
- Bell, E. F., & de Jong, R. S. 2001, *ApJ*, 550, 212
- Benson, B. A., de Haan, T., Dudley, J. P., et al. 2013, *ApJ*, 763, 147
- Bleem, L. E., Stalder, B., Brodwin, M., et al. 2015, *ApJS*, 216, 20
- Bleem, L. E., Stalder, B., de Haan, T., et al. 2015, *ApJS*, 216, 27
- Bocquet, S., Saro, A., Mohr, J. J., et al. 2015, *ApJ*, 799, 214
- Böhringer, H., Voges, W., Huchra, J. P., et al. 2000, *ApJS*, 129, 435
- Borgani, S., Rosati, P., Tozzi, P., et al. 2001, *ApJ*, 561, 13
- Bremer, M. N., Valtchanov, I., Willis, J., et al. 2006, *MNRAS*, 371, 1427
- Brodwin, M., Gonzalez, A. H., Stanford, S. A., et al. 2012, *ApJ*, 753, 162
- Brodwin, M., Greer, C. H., Leitch, E. M., et al. 2015, *ApJ*, 806, 26
- Brodwin, M., McDonald, M., Gonzalez, A. H., et al. 2016, *ApJ*, 817, 122
- Brodwin, M., Stanford, S. A., Gonzalez, A. H., et al. 2013, *ApJ*, 779, 138
- Brodwin, M., Stern, D., Vikhlinin, A., et al. 2011, *ApJ*, 732, 33
- Bruzual, G., & Charlot, S. 2003, *MNRAS*, 344, 1000
- Carlberg, R. G., Yee, H. K. C., Ellingson, E., et al. 1996, *ApJ*, 462, 32
- Carlstrom, J. E., Ade, P. A. R., Aird, K. A., et al. 2011, *PASP*, 123, 568
- Cavaliere, A., & Fusco-Femiano, R. 1976, *A&A*, 49, 137
- de Jong, J. T. A., Verdoes Kleijn, G. A., Kuijken, K. H., & Valentijn, E. A. 2013, *ExA*, 35, 25
- Demarco, R., Rosati, P., Lidman, C., et al. 2005, *A&A*, 432, 381
- Demarco, R., Rosati, P., Lidman, C., et al. 2007, *ApJ*, 663, 164
- Demarco, R., Wilson, G., Muzzin, A., et al. 2010, *ApJ*, 711, 1185
- DES Collaboration, Abbott, T. M. C., Abdalla, F. B., et al. 2018, arXiv:1801.03181
- Dye, S., Warren, S. J., Hambly, N. C., et al. 2006, *MNRAS*, 372, 1227
- Eckert, D., Molendi, S., & Paltani, S. 2011, *A&A*, 526, A79
- Eisenhardt, P. R. M., Brodwin, M., Gonzalez, A. H., et al. 2008, *ApJ*, 684, 905
- Ettori, S., Donnarumma, A., Pointecouteau, E., et al. 2013, *SSRv*, 177, 119
- Fazio, G. G., Hora, J. L., Allen, L. E., et al. 2004, *ApJS*, 154, 10
- Galametz, A., Stern, D., Pentericci, L., et al. 2013, *A&A*, 559, A2
- Galametz, A., Stern, D., Stanford, S. A., et al. 2010, *A&A*, 516, A101
- Gioia, I. M., Maccacaro, T., Schild, R. E., et al. 1990, *ApJS*, 72, 567
- Girardi, L., Barbieri, M., Groenewegen, M. A. T., et al. 2012, *ASSP*, 26, 165
- Girardi, M., Fadda, D., Giuricin, G., et al. 1996, *ApJ*, 457, 61
- Gladders, M. D., & Yee, H. K. C. 2000, *AJ*, 120, 2148
- Gonzalez, A. H., Stanford, S. A., Brodwin, M., et al. 2012, *ApJ*, 753, 163
- Hao, J., McKay, T. A., Koester, B. P., et al. 2010, *ApJS*, 191, 254
- Hasselfield, M., Hilton, M., Marriage, T. A., et al. 2013, *JCAP*, 7, 8
- High, F. W., Hoekstra, H., Leethochawalit, N., et al. 2012, *ApJ*, 758, 68
- Hoekstra, H. 2007, *MNRAS*, 379, 317
- Hoekstra, H., Mahdavi, A., Babul, A., & Bildfell, C. 2012, *MNRAS*, 427, 1298
- Kelly, B. C. 2007, *ApJ*, 665, 1489
- Koester, B. P., McKay, T. A., Annis, J., et al. 2007, *ApJ*, 660, 239
- Laureijs, R., Amiaux, J., Arduini, S., et al. 2011, arXiv:1110.3193
- Liu, J., Hennig, C., Desai, S., et al. 2015, *MNRAS*, 449, 3370
- LSST Science Collaboration, Abell, P. A., Allison, J., et al. 2009, arXiv:0912.0201
- Mahdavi, A., Hoekstra, H., Babul, A., & Henry, J. P. 2008, *MNRAS*, 384, 1567
- Mainzer, A., Bauer, J., Grav, T., et al. 2011, *ApJ*, 731, 53
- Mancone, C. L., Gonzalez, A. H., Brodwin, M., et al. 2010, *ApJ*, 720, 284
- Mann, A. W., & Ebeling, H. 2012, *MNRAS*, 420, 2120
- Mantz, A., Allen, S. W., Ebeling, H., Rapetti, D., & Drlica-Wagner, A. 2010, *MNRAS*, 406, 1773
- Mantz, A. B., Abdulla, Z., Carlstrom, J. E., et al. 2014, *ApJ*, 794, 157
- Maughan, B. J. 2007, *ApJ*, 668, 772
- Maughan, B. J., Giles, P. A., Randall, S. W., Jones, C., & Forman, W. R. 2012, *MNRAS*, 421, 1583
- Melchior, P., Gruen, D., McClintock, T., et al. 2017, *MNRAS*, 469, 4899
- Menanteau, F., Hughes, J. P., Barrientos, L. F., et al. 2010, *ApJS*, 191, 340
- Mercurio, A., Girardi, M., Boschin, W., Merluzzi, P., & Busarello, G. 2003, *A&A*, 397, 431

- Muzzin, A., Wilson, G., Demarco, R., et al. 2013, *ApJ*, 767, 39
- Pacaud, F., Pierre, M., Adami, C., et al. 2007, *MNRAS*, 382, 1289
- Papovich, C. 2008, *ApJ*, 676, 206
- Pierre, M., Pacaud, F., Juin, J. B., et al. 2011, *MNRAS*, 414, 1732
- Piffaretti, R., Arnaud, M., Pratt, G. W., Pointecouteau, E., & Melin, J.-B. 2011, *A&A*, 534, A109
- Planck Collaboration, Aghanim, N., Arnaud, M., et al. 2011, *A&A*, 536, A9
- Planck Collaboration, Ade, P. A. R., Aghanim, N., et al. 2014, *A&A*, 571, A29
- Planck Collaboration, Ade, P. A. R., Aghanim, N., et al. 2015, *A&A*, 581, A14
- Press, W. H., & Schechter, P. 1974, *ApJ*, 187, 425
- Press, W. H., Teukolsky, S. A., Vetterling, W. T., & Flannery, B. P. 2002, *Numerical Recipes in C++: The Art of Scientific Computing* (Cambridge: Cambridge Univ. Press)
- Reichert, A., Böhringer, H., Fassbender, R., & Mühlegger, M. 2011, *A&A*, 535, A4
- Rettura, A., Martinez-Manso, J., Stern, D., et al. 2014, *ApJ*, 797, 109
- Rettura, A., Mei, S., Stanford, S. A., et al. 2011, *ApJ*, 732, 94
- Rettura, A., Rosati, P., Nonino, M., et al. 2010, *ApJ*, 709, 512
- Rettura, A., Rosati, P., Strazzullo, V., et al. 2006, *A&A*, 458, 717
- Rossetti, M., Gastaldello, F., Ferioli, G., et al. 2016, *MNRAS*, 457, 4515
- Rozo, E., Bartlett, J. G., Evrard, A. E., & Rykoff, E. S. 2014a, *MNRAS*, 438, 78
- Rozo, E., Evrard, A. E., Rykoff, E. S., & Bartlett, J. G. 2014b, *MNRAS*, 438, 62
- Rozo, E., Rykoff, E. S., Koester, B. P., et al. 2009, *ApJ*, 703, 601
- Rozo, E., Wechsler, R. H., Rykoff, E. S., et al. 2010, *ApJ*, 708, 645
- Rykoff, E. S., Koester, B. P., Rozo, E., et al. 2012, *ApJ*, 746, 178
- Rykoff, E. S., Rozo, E., Busha, M. T., et al. 2014, *ApJ*, 785, 104
- Sanderson, A. J. R., Edge, A. C., & Smith, G. P. 2009, *MNRAS*, 398, 1698
- Saro, A., Bocquet, S., Rozo, E., et al. 2015, *MNRAS*, 454, 2305
- Sartoris, B., Biviano, A., Fedeli, C., et al. 2016, *MNRAS*, 459, 1764
- Serenio, M. 2015, *MNRAS*, 450, 3665
- Stanford, S. A., Brodwin, M., Gonzalez, A. H., et al. 2012, *ApJ*, 753, 164
- Staniszewski, Z., Ade, P. A. R., Aird, K. A., et al. 2009, *ApJ*, 701, 32
- Story, K. T., Reichardt, C. L., Hou, Z., et al. 2013, *ApJ*, 779, 86
- Sunyaev, R. A., & Zeldovich, Y. B. 1972, *CoASP*, 4, 173
- Surace, J., Shupe, D. L., Fang, F., et al. 2004, *The SWIRE N1 Image Atlases and Source Catalogs* (Pasadena, CA: Spitzer Science Center)
- Tremaine, S., Gebhardt, K., Bender, R., et al. 2002, *ApJ*, 574, 740
- Umetsu, K., Medezinski, E., Nonino, M., et al. 2014, *ApJ*, 795, 163
- Viana, P. T. P., & Liddle, A. R. 1999, *MNRAS*, 303, 535
- Vikhlinin, A., Burenin, R. A., Ebeling, H., et al. 2009, *ApJ*, 692, 1033
- Vikhlinin, A., McNamara, B. R., Forman, W., et al. 1998, *ApJ*, 502, 558
- Voges, W., Aschenbach, B., Boller, T., et al. 1999, *A&A*, 349, 389
- von der Linden, A., Mantz, A., Allen, S. W., et al. 2014, *MNRAS*, 443, 1973
- Šuhada, R., Song, J., Böhringer, H., et al. 2012, *A&A*, 537, A39
- Wainscoat, R. J., Cohen, M., Volk, K., Walker, H. J., & Schwartz, D. E. 1992, *ApJS*, 83, 111
- Wen, Z. L., Han, J. L., & Liu, F. S. 2012, *ApJS*, 199, 34
- White, S. D. M., Efstathiou, G., & Frenk, C. S. 1993, *MNRAS*, 262, 1023
- Wilson, G., Muzzin, A., Yee, H. K. C., et al. 2009, *ApJ*, 698, 1943
- Wright, E. L., Eisenhardt, P. R. M., Mainzer, A. K., et al. 2010, *AJ*, 140, 1868
- Wylezalek, D., Galametz, A., Stern, D., et al. 2013, *ApJ*, 769, 79
- Yee, H. K. C., & Ellingson, E. 2003, *ApJ*, 585, 215
- Yee, H. K. C., & López-Cruz, O. 1999, *AJ*, 117, 1985
- York, D. G., Adelman, J., Anderson, J. E., Jr., et al. 2000, *AJ*, 120, 1579
- Zeimann, G. R., Stanford, S. A., Brodwin, M., et al. 2012, *ApJ*, 756, 115
- Zwicky, F., & Kowal, C. T. 1968, in *Catalogue of Galaxies and of Clusters of Galaxies*, Vol. 6 (Pasadena, CA: California Institute of Technology), CGCG6